nature cardiovascular research

Supplementary information

https://doi.org/10.1038/s44161-026-00882-8

# All-fiber wireless auscultation garment for cardiopulmonary diagnostics

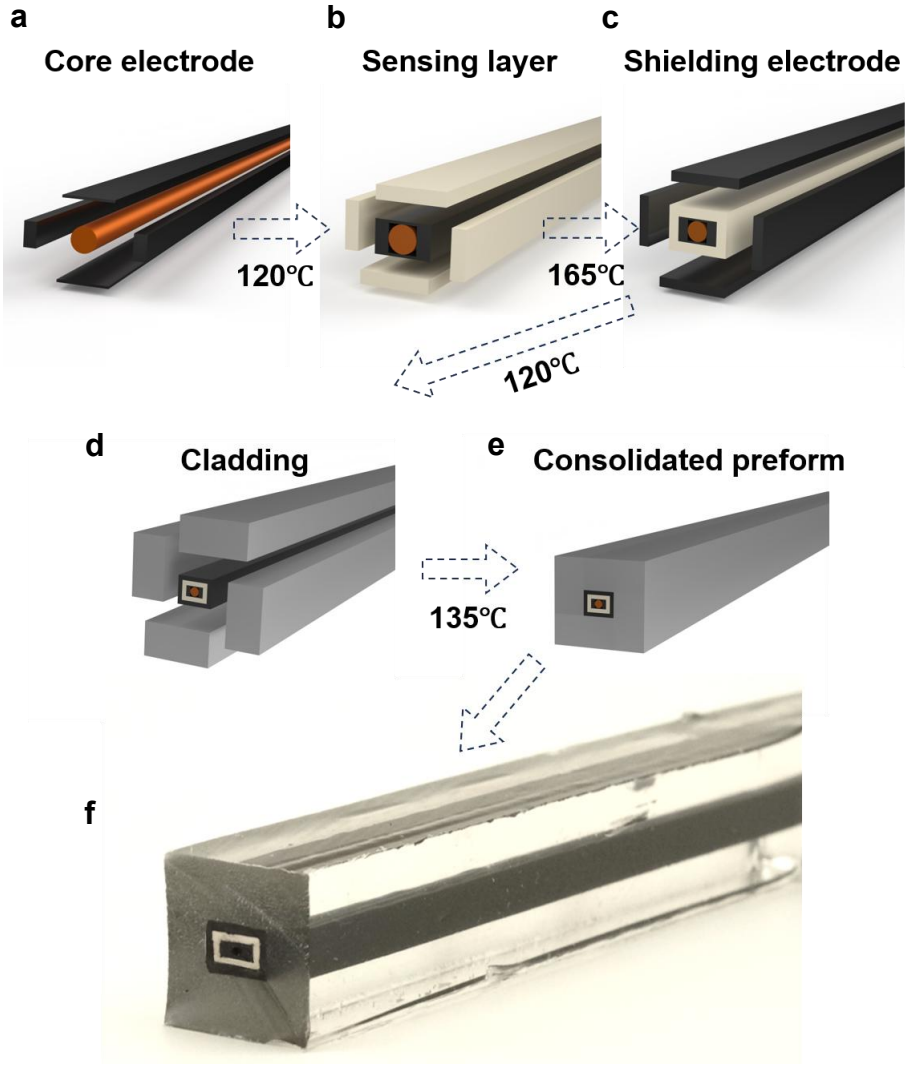
In the format provided by the authors and unedited

## The Supplementary file includes:

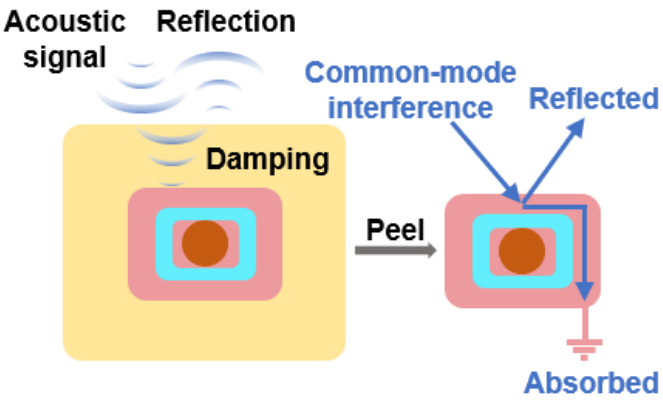
Supplementary Figure 1 to 48

Supplementary Tables 1 to 3

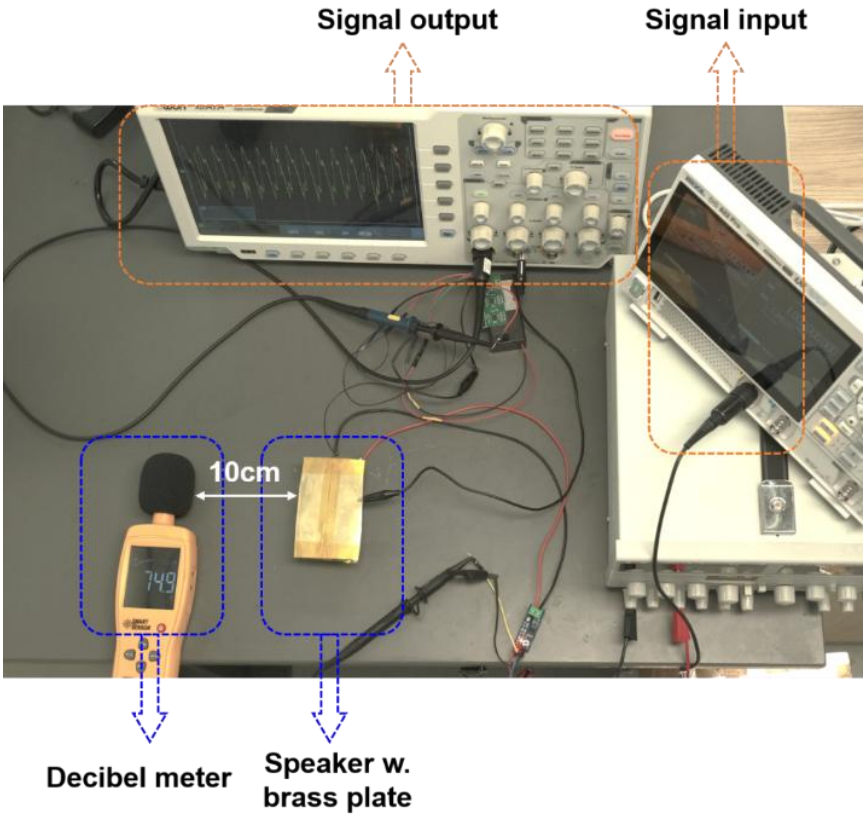
Supplementary Videos 1 to 8



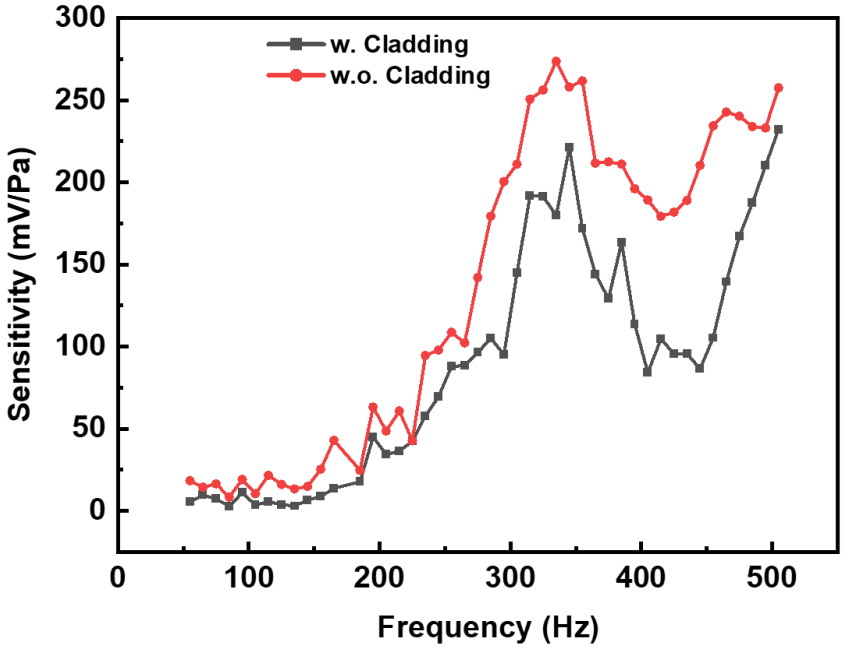

**Supplementary Figure 1. Schematic of FCM preform manufacturing process. a**, The core electrode constructed using a 1 mm diameter straight PTFE-coated spring steel wire as a central spacer, flanked on both sides by 1 mm × 0.5 mm pre-cut CPE strips. To prevent deformation of the piezoelectric layer during thermal drawing by central copper wire because of the direct contact, a 100 μm-thick CPE film was placed above and below the assembly. The entire structure was then consolidated by hot pressing at 120 °C. **b**, The surrounding piezoelectric layer composed of four pre-cut PVDF-TrFE-PZT composite strips: 1.7 mm × 0.5 mm on the left and right sides, and 2.5 mm × 0.5 mm on the top and bottom. The assembled structure was then consolidated by hot pressing at 165 °C. **c**, The shielding electrode composed of four pre-cut CPE strips: 2.7 mm × 0.5 mm on the left and right sides, and 3.5 mm × 0.5 mm on the top and bottom. The assembled structure was then consolidated by hot pressing at 165 °C. **d**, The whole structure using 4mm SEBS thickness pre-cut CPE strips to protect, then use 135 °C for final consolidation. **e**, Final assembled preform structure. **f**, Photograph of the preform, with the central spring steel wire removed to create a 1 mm channel for copper wire insertion during thermal drawing. Scale bar, 5mm (**f**).



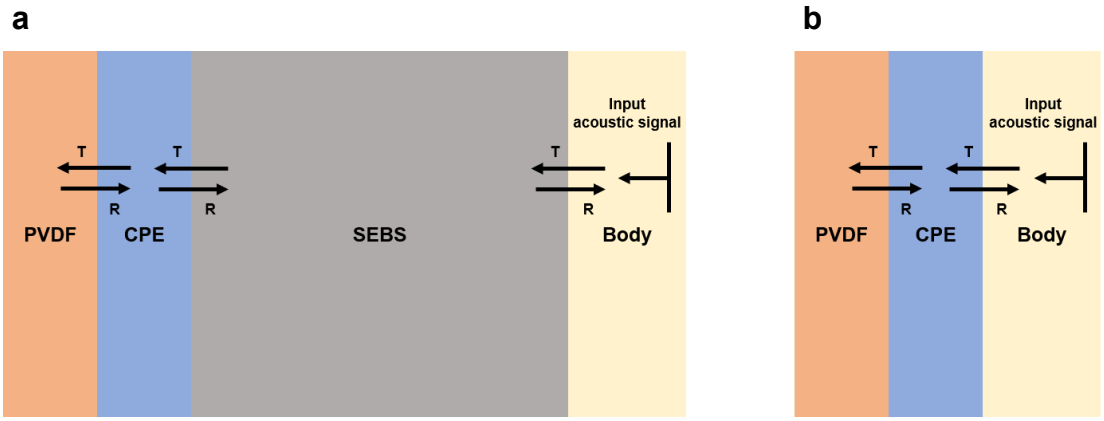

**Supplementary Figure 2. Illustration of the FCM structure, showing key advantages:** The removal of cladding (e.g. SEBS) is necessary to prevent acoustic signal damping caused by acoustic impedance mismatch, and common-mode interference from surrounding and human skin is absorbed to the ground or reflected by shielding electrode.



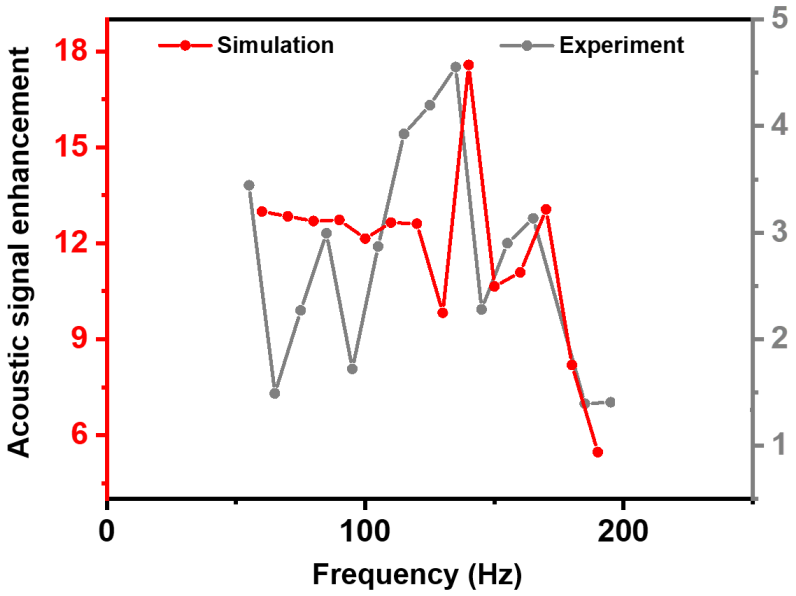

**Supplementary Figure 3. The frequency response test setup simulating the contact microphone configuration.**



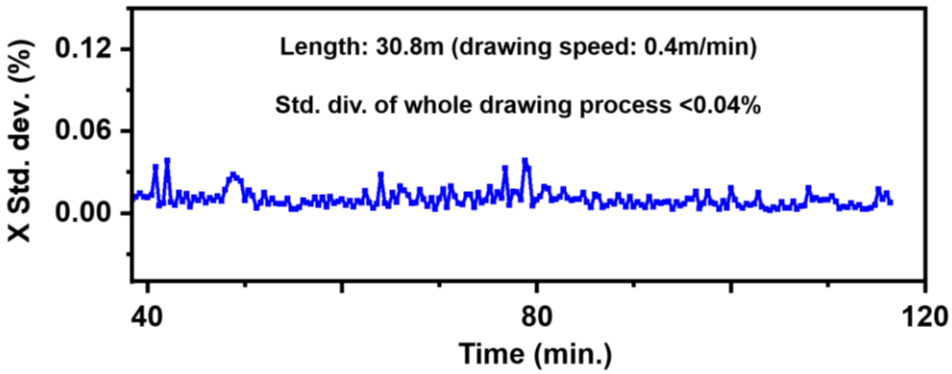

**Supplementary Figure 4. 8 cm fibre sensitivity comparison with and without soft cladding over the 55–505 Hz frequency range.**



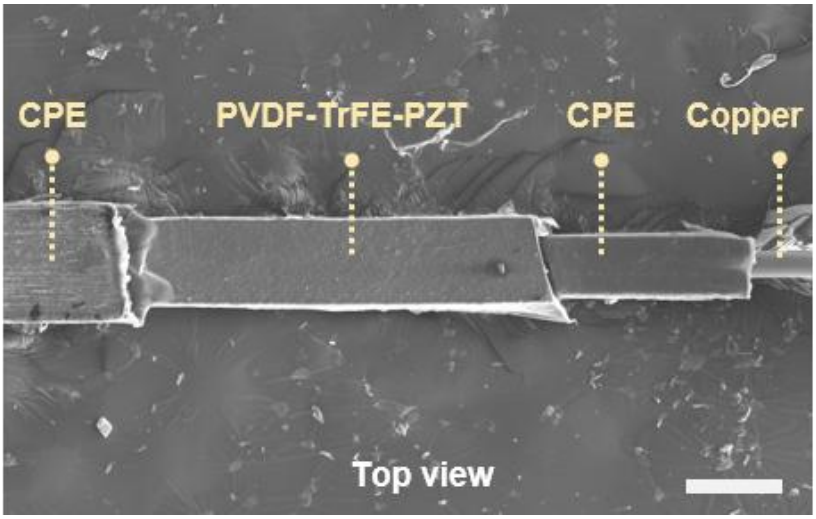

**Supplementary Figure 5. Schematic of acoustic propagation in the Body-SEBS-CPE (a)** and Body-CPE **(b)** modeling structure**.**



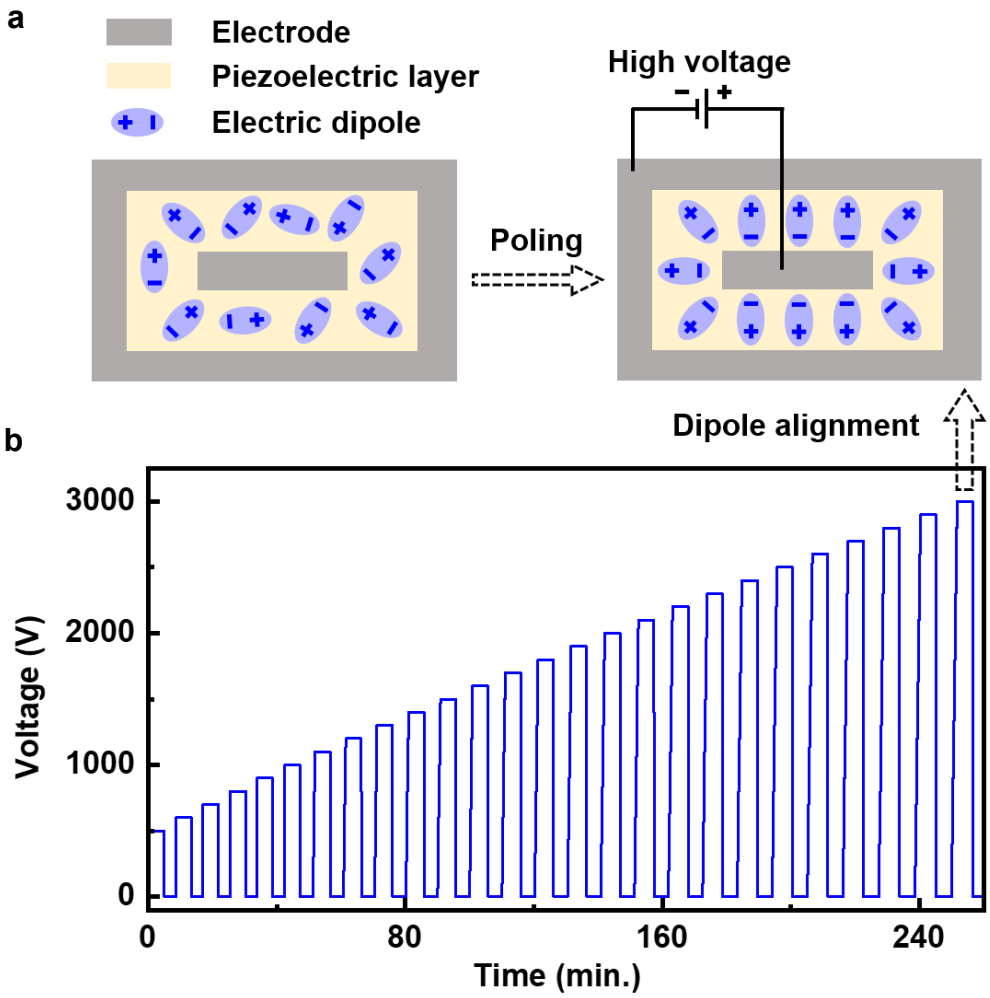

**Supplementary Figure 6. Simulation and experimental results of acoustic signal enhancement achieved through acoustic impedance matching via material selection in the fibre matrix, demonstrated by the profile agreement between modeled and measured responses.**



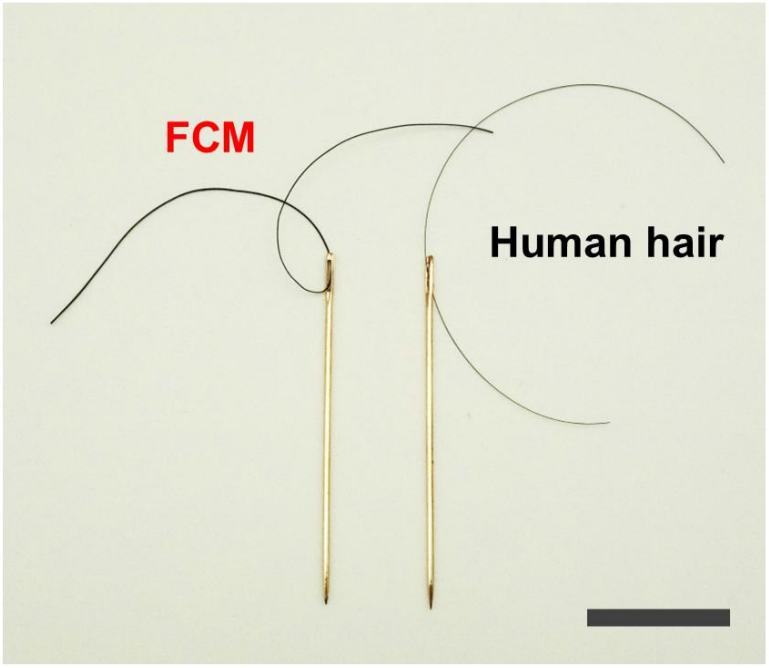

**Supplementary Figure 7. Thermal drawing data of FCM.** After an initial stabilization period (38 mins) during thermal drawing, the fibre maintained a standard deviation of less than 0.04% in cross-sectional dimensions throughout the remainder of the process. With a drawing speed of 0.4 m/min, a single continuous draw yielded 30.8 meters of dimensionally stable fibre.



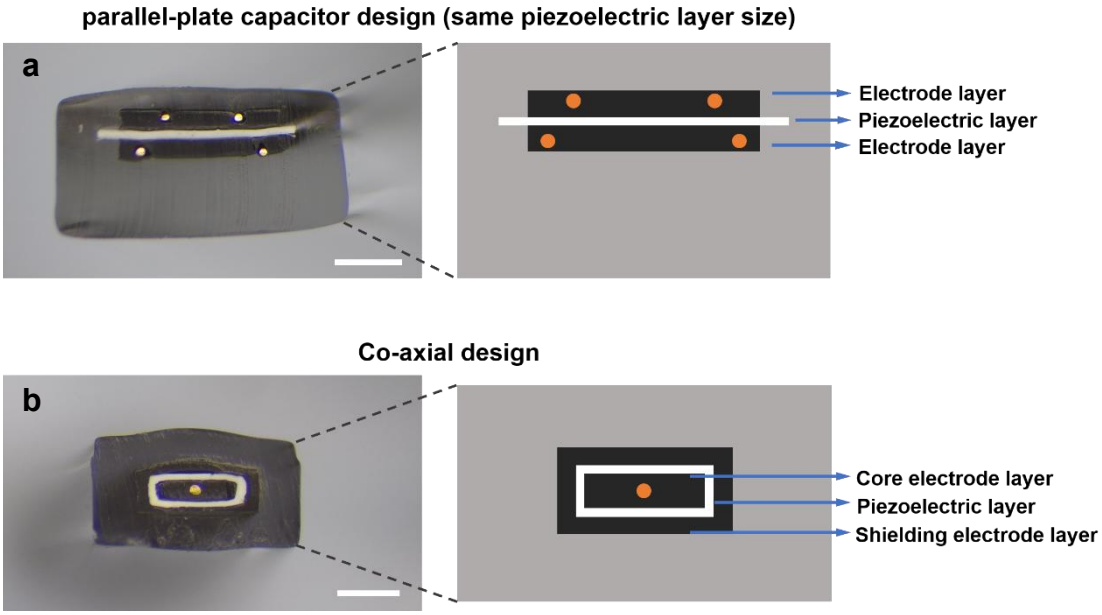

**Supplementary Figure 8. SEM micrograph of the fibre top view, showing that the sensor layer and electrode layers remain distinctly separated.** Representative SEM image from n = 3 independently prepared fibre samples, with similar results. Scale bar, 150 μm.



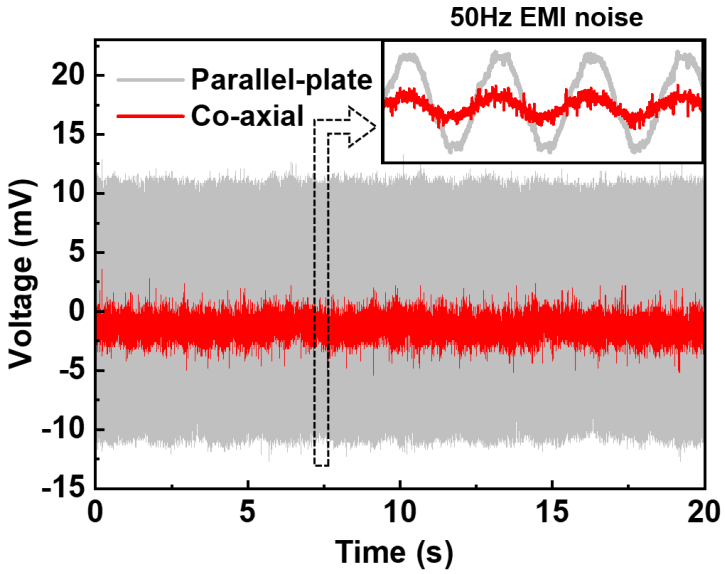

**Supplementary Figure 9. Poling process of FCM. a**, Schematic of the poling process for the co-axial FCM. Upon applying a stepwise voltage increase up to 3 kV (equivalent to 120 V/μm), the electric dipoles within the piezoelectric layer align along the electric field direction, resulting in a functional piezoelectric response. **b**, Applied voltage profile of the stepwise oil-bath poling process, showing gradual voltage increments from 500 V to 3 kV in 100 V steps.



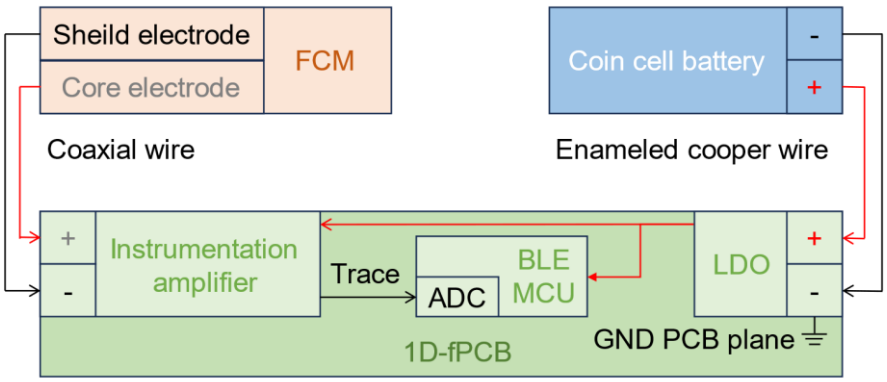

**Supplementary Figure 10. Photograph of a piece of fibre contact microphone and human hair, showing the fibre hundred-um level thickness and flexibility.** Scale bar, 2 cm.



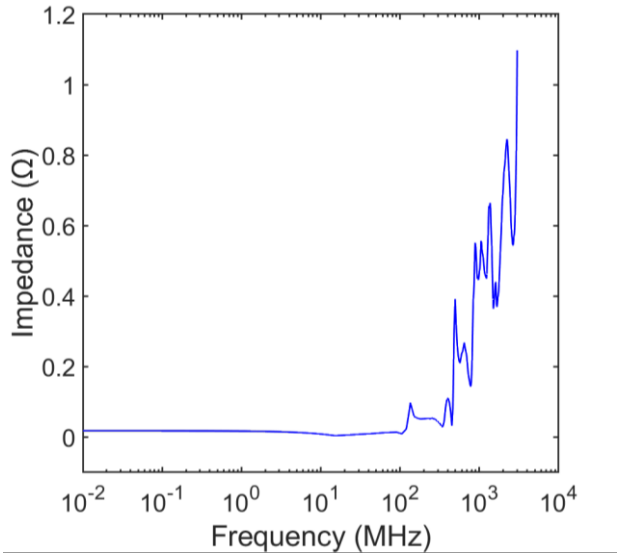

**Supplementary Figure 11. Cross-sectional views of the fibres used for raw signal comparison between the parallel-plate capacitor design and the co-axial design. a**, Schematic and optical micrograph of the parallel-plate capacitor design. **b**, Schematic and optical micrograph of the co-axial design. To eliminate the influence of piezoelectric layer area differences, the co-axial design was fabricated with an expanded piezoelectric layer to match the surface area of the parallel-plate capacitor design. n = 3 independently prepared fibres per design. Scale bar, 400μm (**a**), 300μm (**b**).



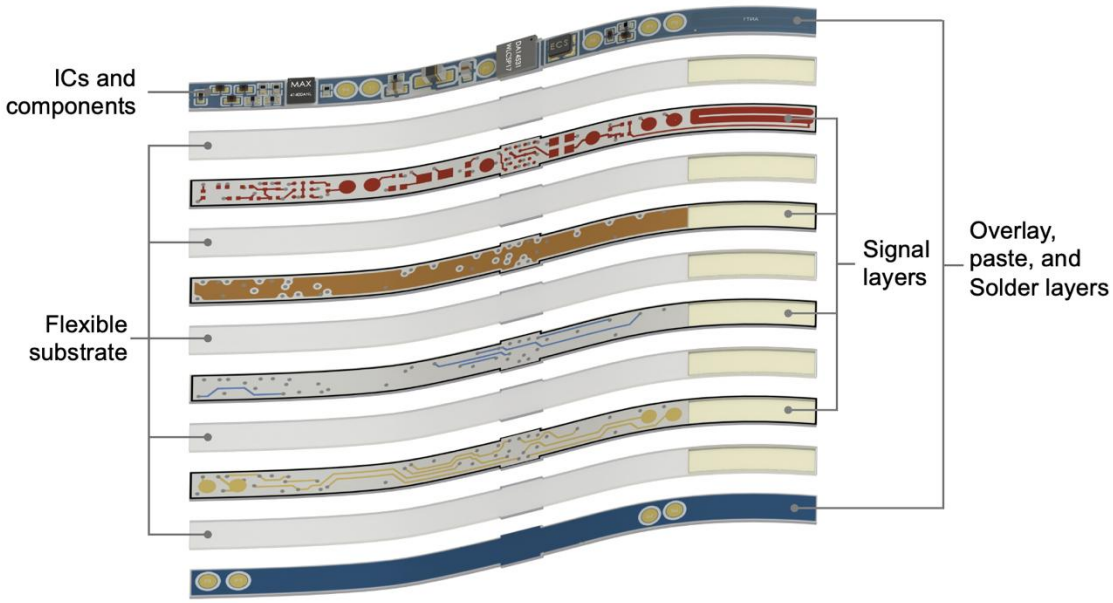

**Supplementary Figure 12. Baseline noise levels of both designs without skin contact.** Two fibres of equal length were placed on a tabletop and connected to the same oscilloscope. The co-axial design demonstrates superior capability in blocking electromagnetic interference (EMI) from surrounding equipment, as evidenced by its significantly lower 50 Hz baseline noise.



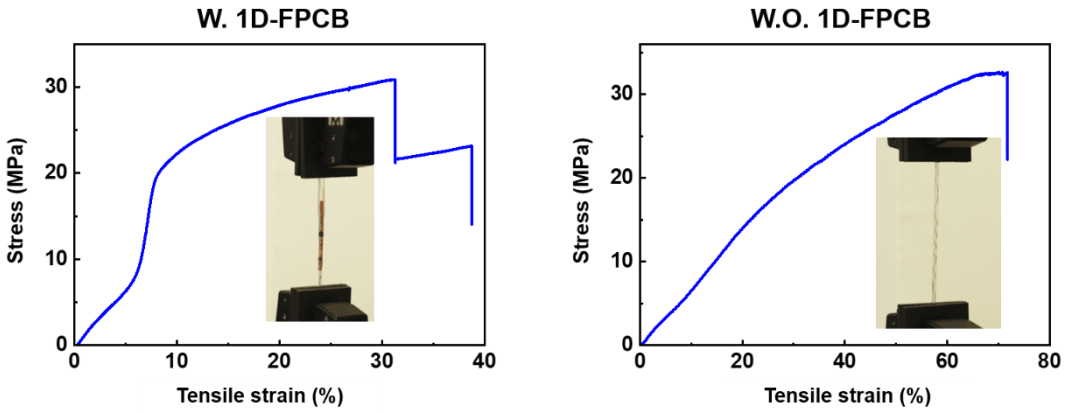

**Supplementary Figure 13. FiWAS electric connection schematic.**



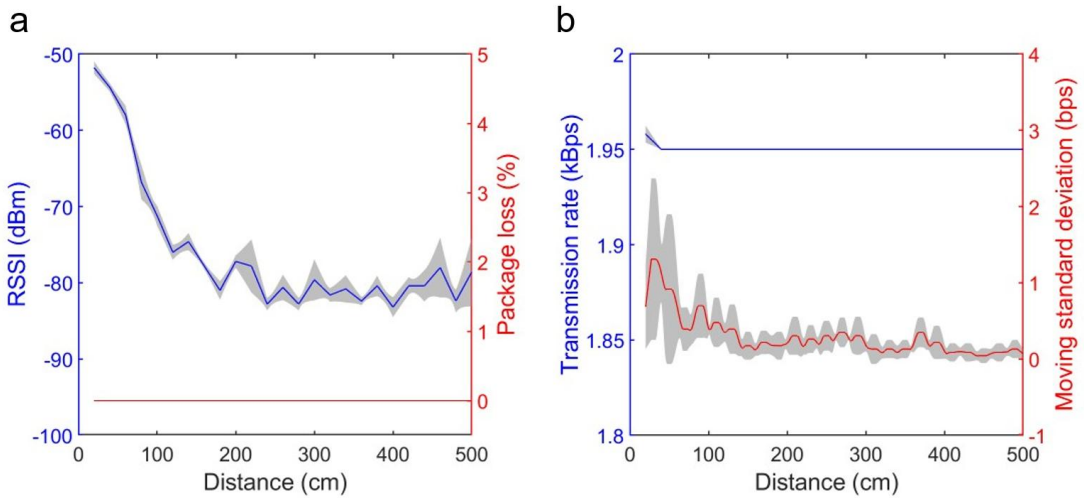

**Supplementary Figure 14. 1D-fPCB ground plane impedance.**



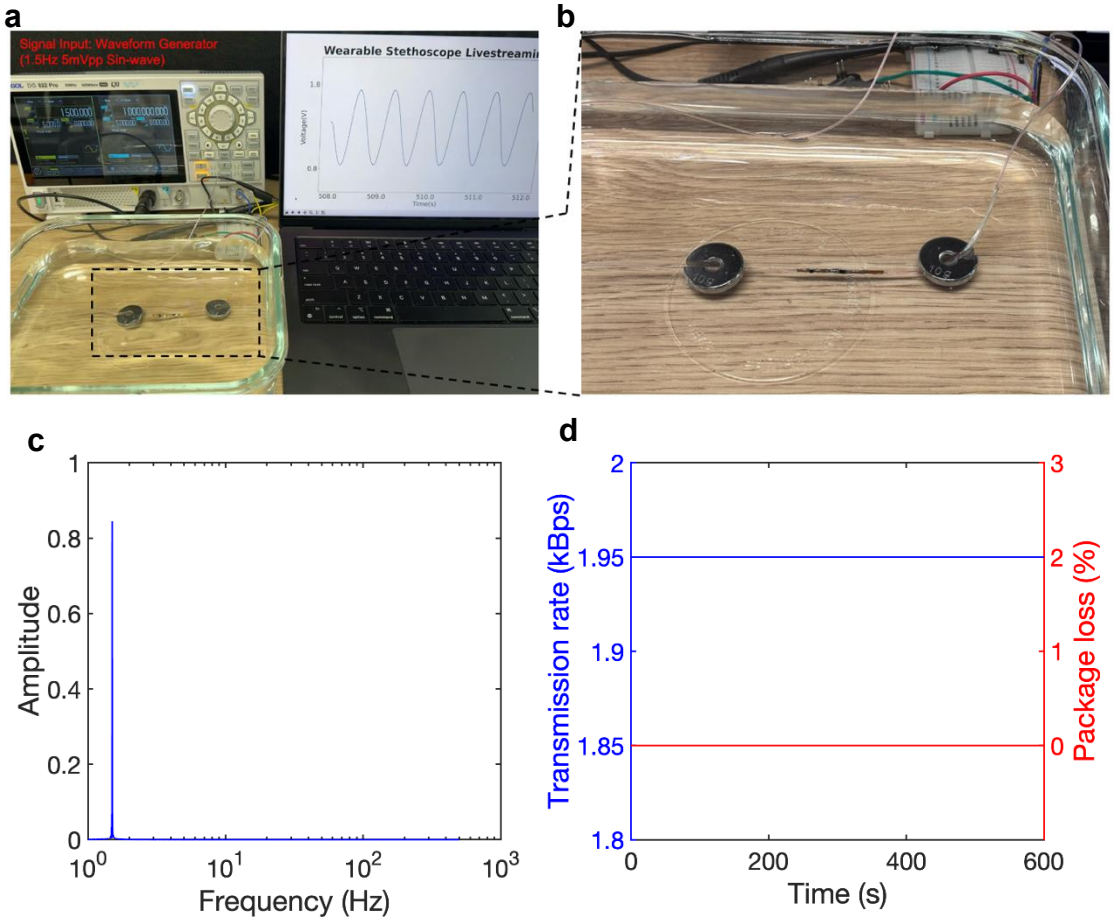

**Supplementary Figure 15. Structure of the 1D fPCB.** At the top are the integrated circuits (ICs) and electronic components mounted on the surface, forming the functional part of the system. Beneath them are multiple signal layers that route electrical signals, power, and ground through intricately patterned conductive traces. These layers are interleaved and connected to support high-density and multi-directional signal routing. The entire structure is built on a flexible substrate made from polyimide, allowing the PCB to conform to curved or compact surfaces. Surrounding the signal layers are the overlay, solder paste, and solder layers, which together form the top and bottom surfaces of the PCB and provide electrical insulation, mechanical support for surface-mounted components, and reliable electrical connections.



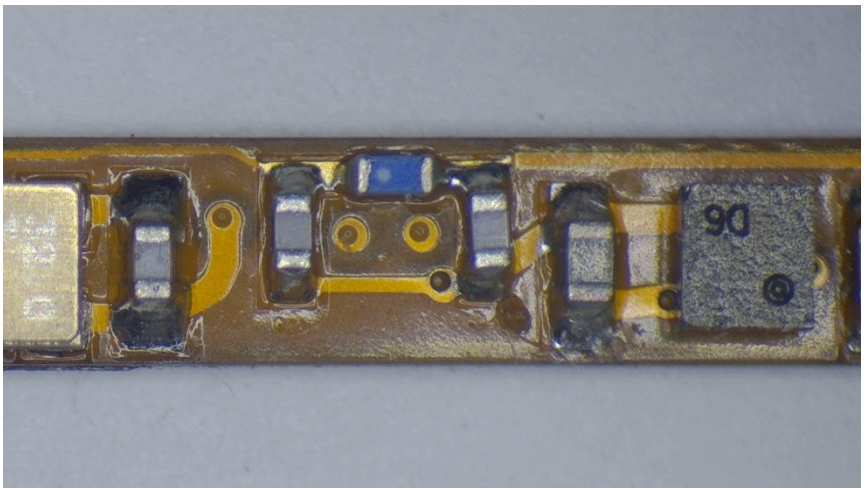

**Supplementary Figure 16. Stress–strain curves of fibre computer.** Breaking point of the 1D-fPCB (left) is one of the soldering nodes on PCB. Breaking point of the fibre (right) is one of the copper wires, showing the soldering node fracture stress (31.2 MPa) is similar to the fracture stress of connecting wire inside the fibre computer (32.6 MPa).



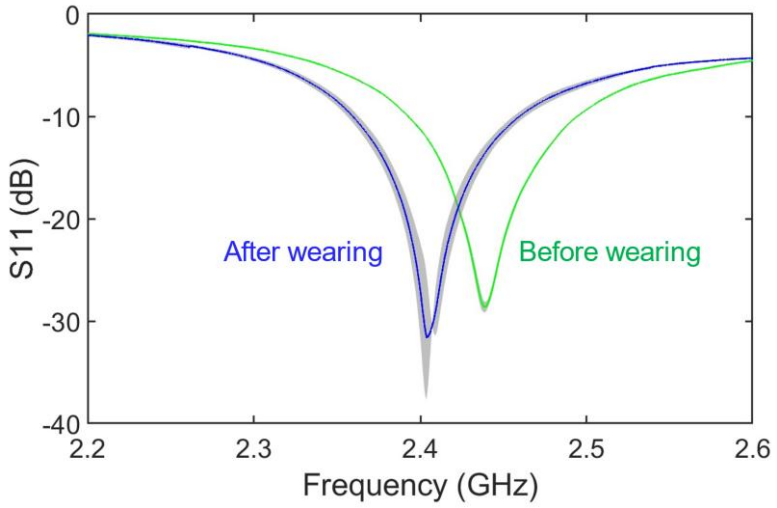

**Supplementary Figure 17. BLE link reliability characterisation in open indoor environment with ECOC cladding. a,** RSSI and package loss performance at different distance, with grey shaded area representing error band. **b,** Transmission rate and its volatility performance at different distance, with grey shaded area representing error band. Lines show the mean and grey shaded bands indicate s.d.; n = 5 independent measurements at each distance.



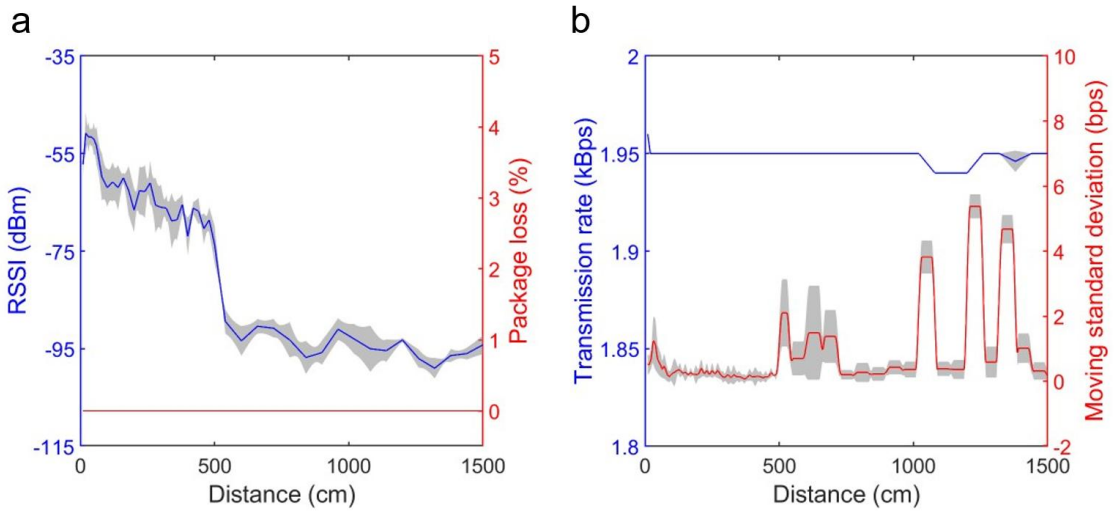

**Supplementary Figure 18. Waterproof characterization of fibre computer. a**, Photograph of the test setup showing the submerged fibre computer receiving a signal (1.5Hz 5mVpp sinusoidal wave) from a waveform generator and wirelessly transmitting data to the Python-based livestreaming upper computer program. **b**, Close-up photograph of the 1D-fPCB section of the fibre computer fully immersed in water. **c,** Fast Fourier Transformation analysis of the data received by host computer, indicating data has no distortion. **d,** Transmission rate and package loss performance during the 10-mins waterproof test, indicating there is no data loss.



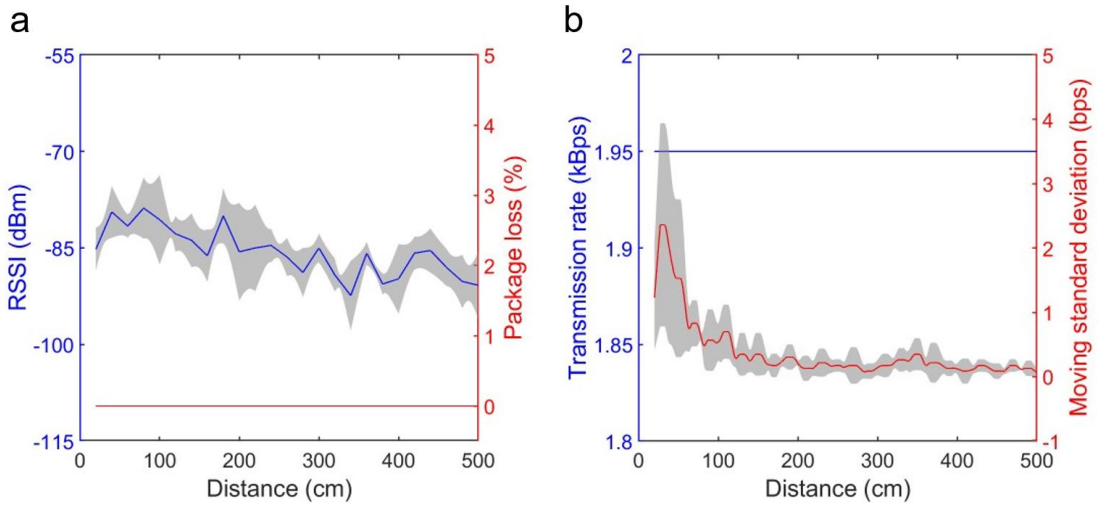

**Supplementary Figure 19. π-type matching network for the Meandered Inverted-F Antenna on 1D-fPCB.**



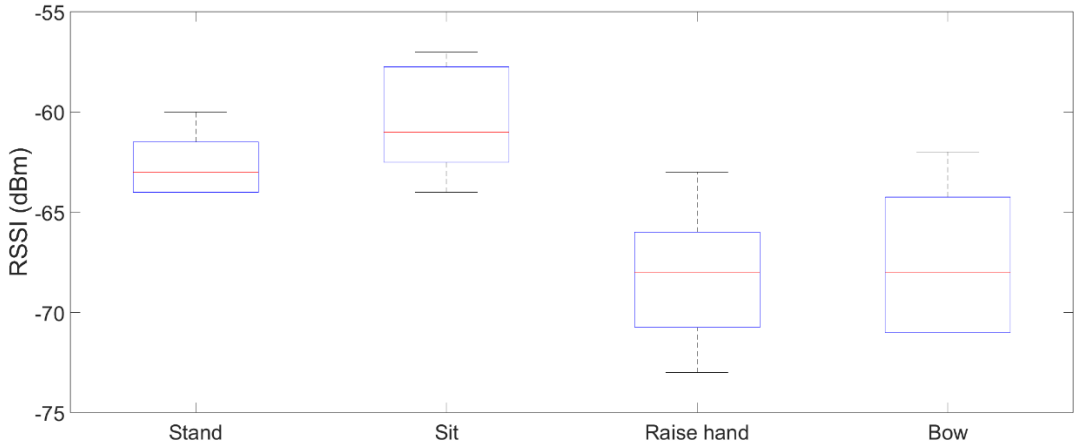

**Supplementary Figure 20. Return loss characterisation of the 1D-fPCB antenna with and without body detuning.** Data are presented as mean ± s.d. from n = 3 independent measurements.



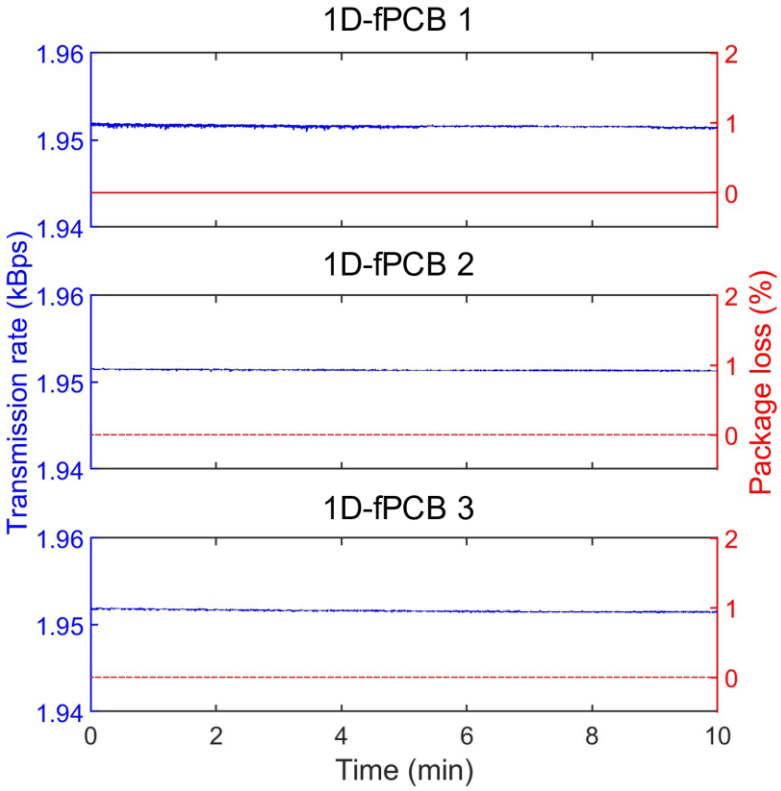

**Supplementary Figure 21. BLE link reliability characterisation in open indoor environment. a,** RSSI and package loss performance at different distance, with grey shaded area representing error band. **b,** Transmission rate and its volatility performance at different distance, with grey shaded area representing error band. Lines show the mean and grey shaded bands indicate s.d.; n = 5 independent measurements at each distance.



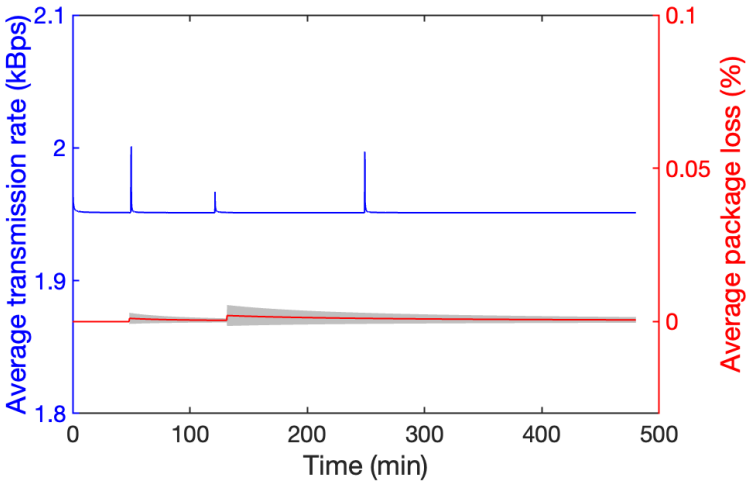

**Supplementary Figure 22. BLE link reliability characterisation in open indoor environment with body shadowing. a,** RSSI and package loss performance at different distance, with grey shaded area representing error band. **b,** Transmission rate and its volatility performance at different distance, with grey shaded area representing error band. Lines show the mean and grey shaded bands indicate s.d.; n = 5 independent measurements at each distance.



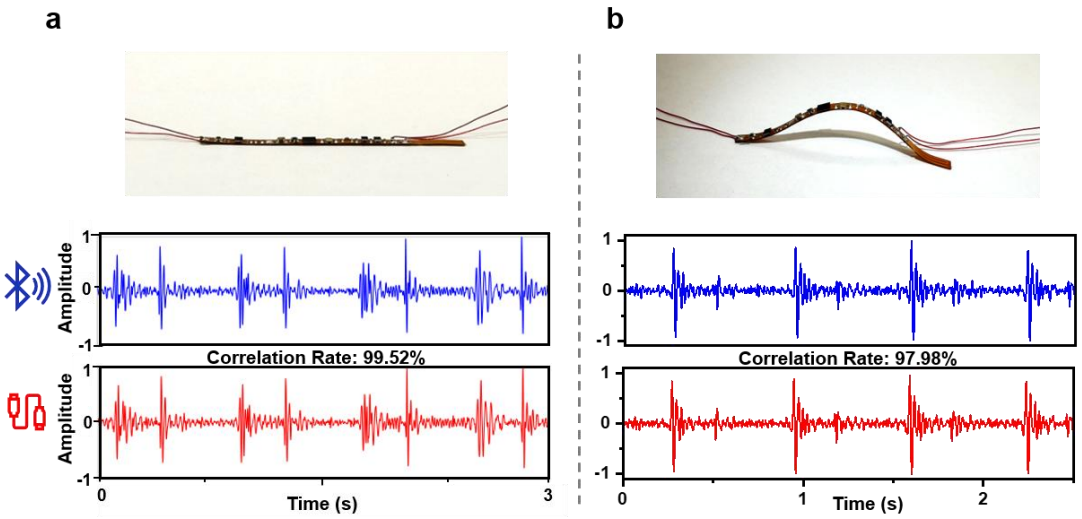

**Supplementary Figure 23. 1D-fPCB BLE RSSI performance under different body posture.** Boxes indicate the 25%–75% range, whiskers indicate the minimum and maximum values, and horizontal lines indicate the median. Data were obtained from n = 5 independent measurements per posture.



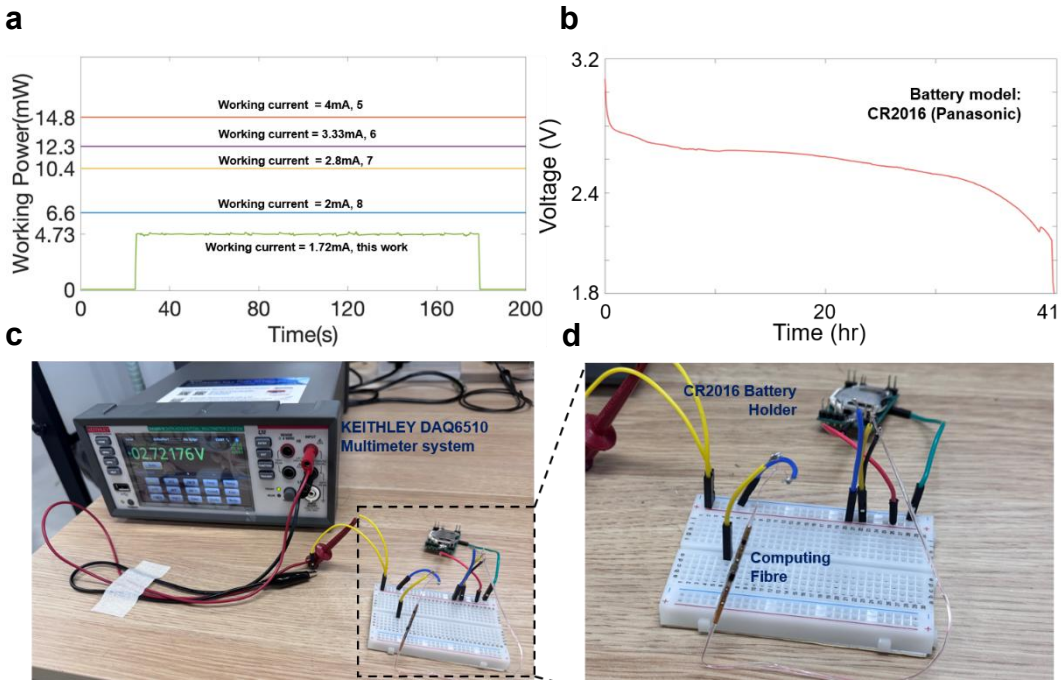

**Supplementary Figure 24. Multi-fPCB BLE synchronized transmission interference characterisation.**



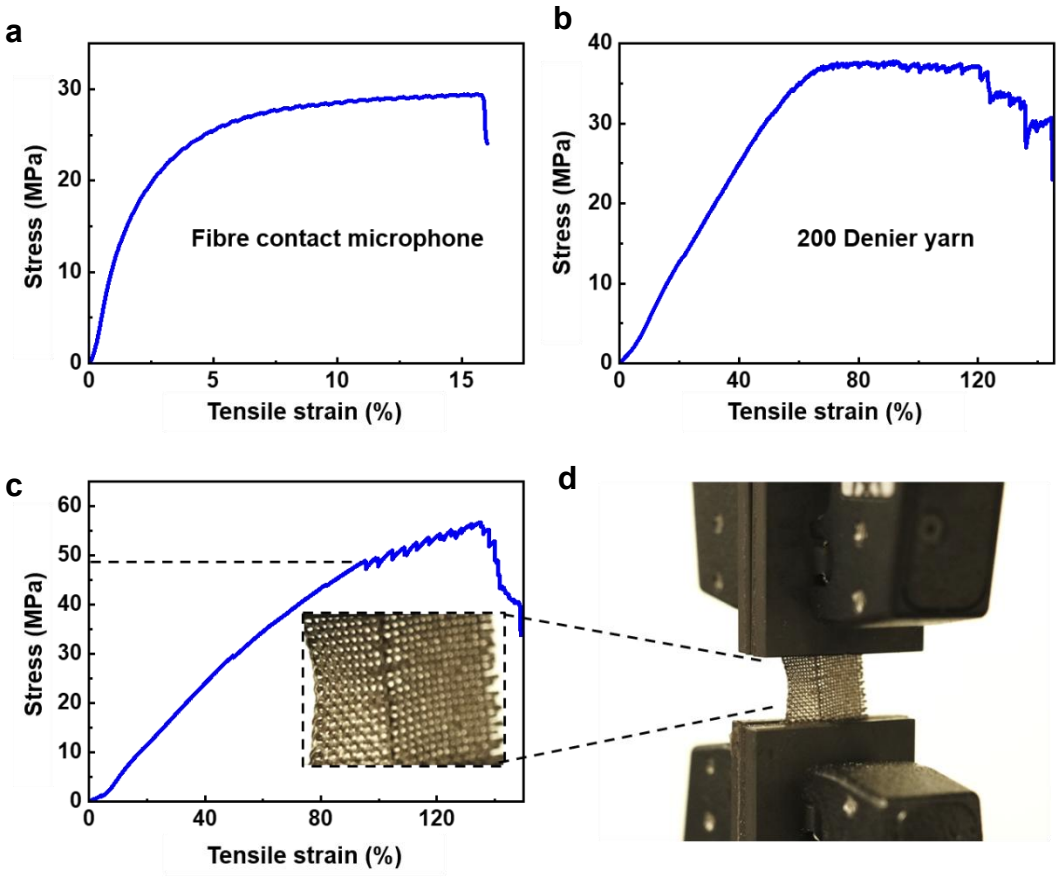

**Supplementary Figure 25. FiWAS long-time on-body wireless operation stability characterisation, with shaded area representing error band.** Lines show the mean and shaded bands indicate s.d.; n = 3 independent measurements.



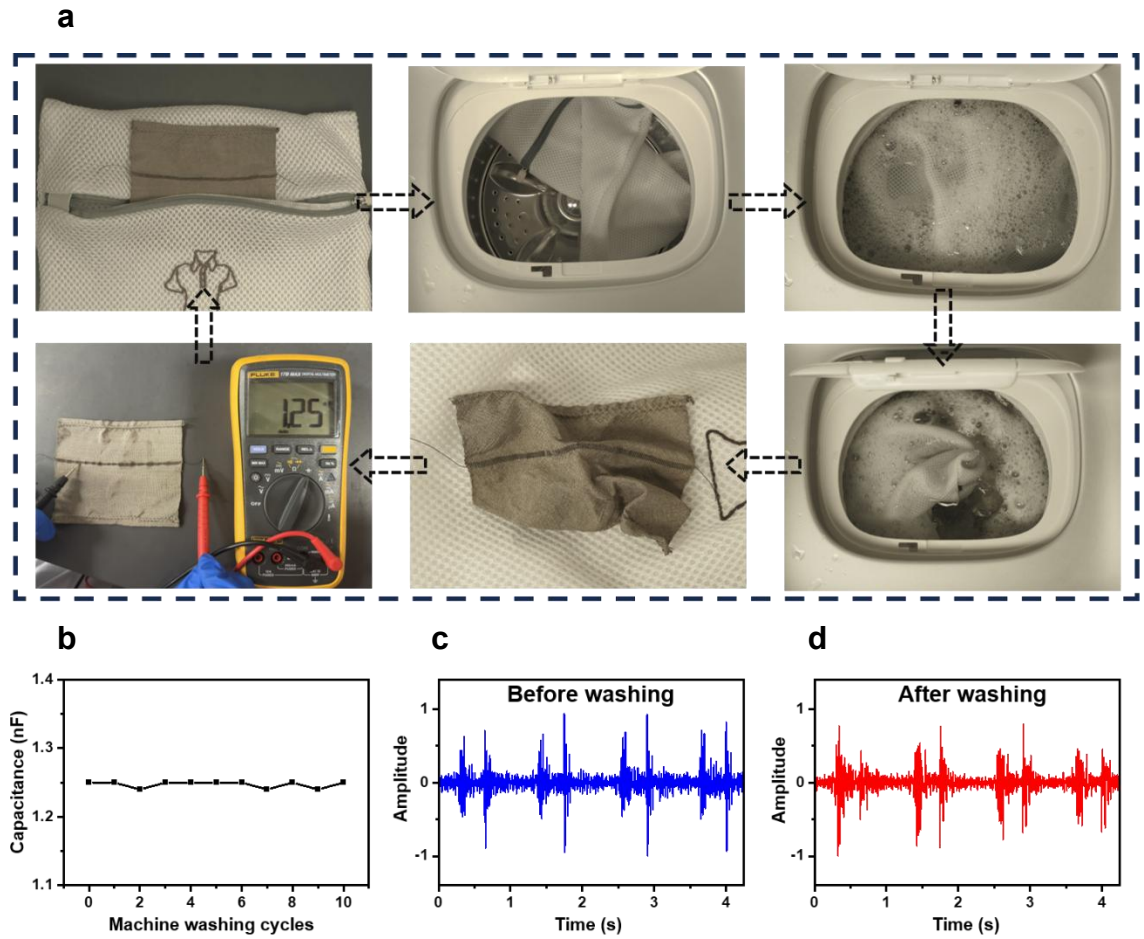

**Supplementary Figure 26. The wireless signals remain highly consistent with wired oscilloscope measurements under both flat (a, 99.52%) and bent (b, 97.98%) conditions, indicating robust transmission fidelity of the 1D-FPCB.**



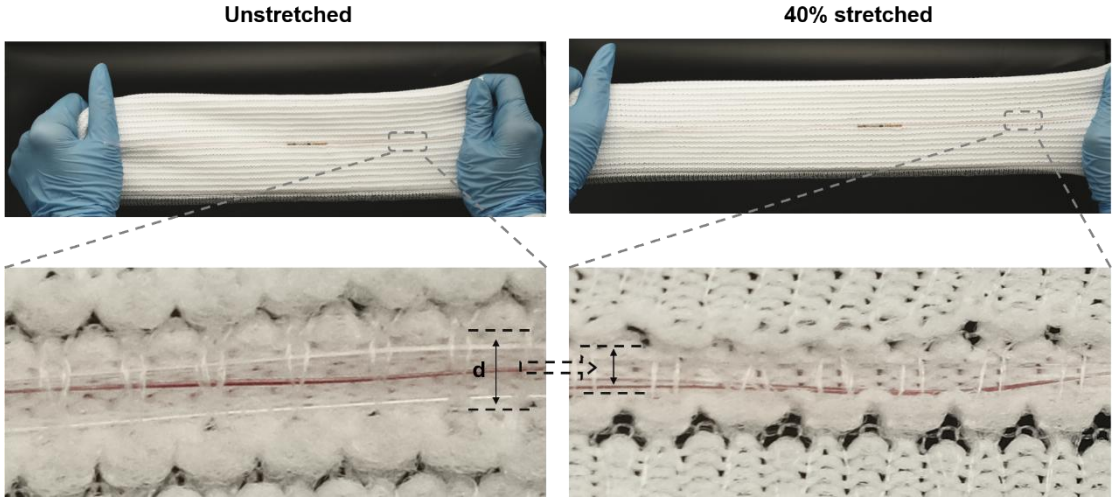

**Supplementary Figure 27. Power consumption characterization of the fibre computer. a**, Comparison of power consumption between the fibre computer and representative MEMS-microphone-based wearable auscultation technologies, as described in Methods. **b**, Residual battery voltage as a function of operating time, starting with a new coin-cell battery (CR2016, Panasonic). **c**, Photograph of the test setup. **d**, Close-up photograph of the fibre computer's electrical connection used for power-consumption characterization.



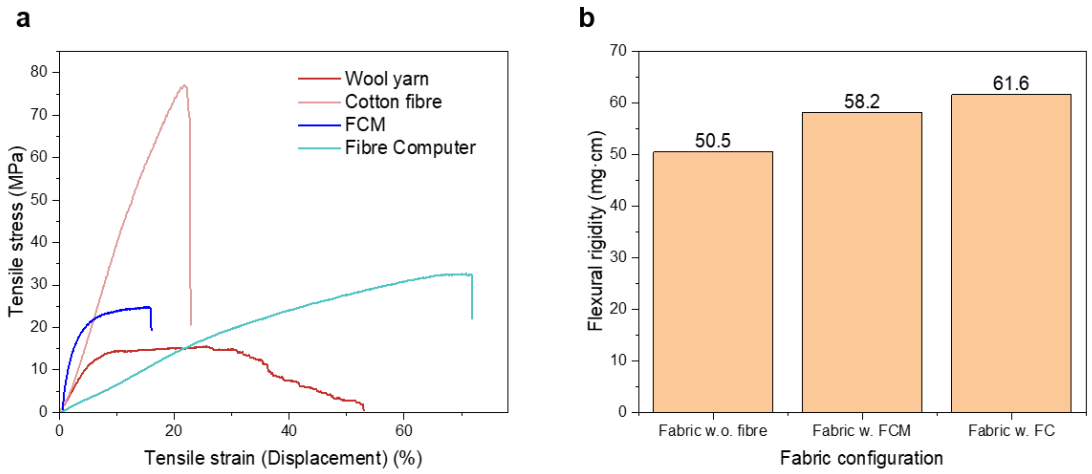

**Supplementary Figure 28. Stress–strain curves of the single FCM (a**), 200 denier nylon yarn **(b),** and the woven fabric incorporating one FCM **(c,d).** The FCM exhibits a fracture strength of 29.7 MPa, compared to 38.5 MPa for the 200 Denier yarn. When integrated into a woven structure, the overall tensile strength is enhanced, with the FCM's effective fracture strength increasing to 48.8 MPa. In the fabric tensile test, it remains the first to break due to act as the mechanically weakest component.



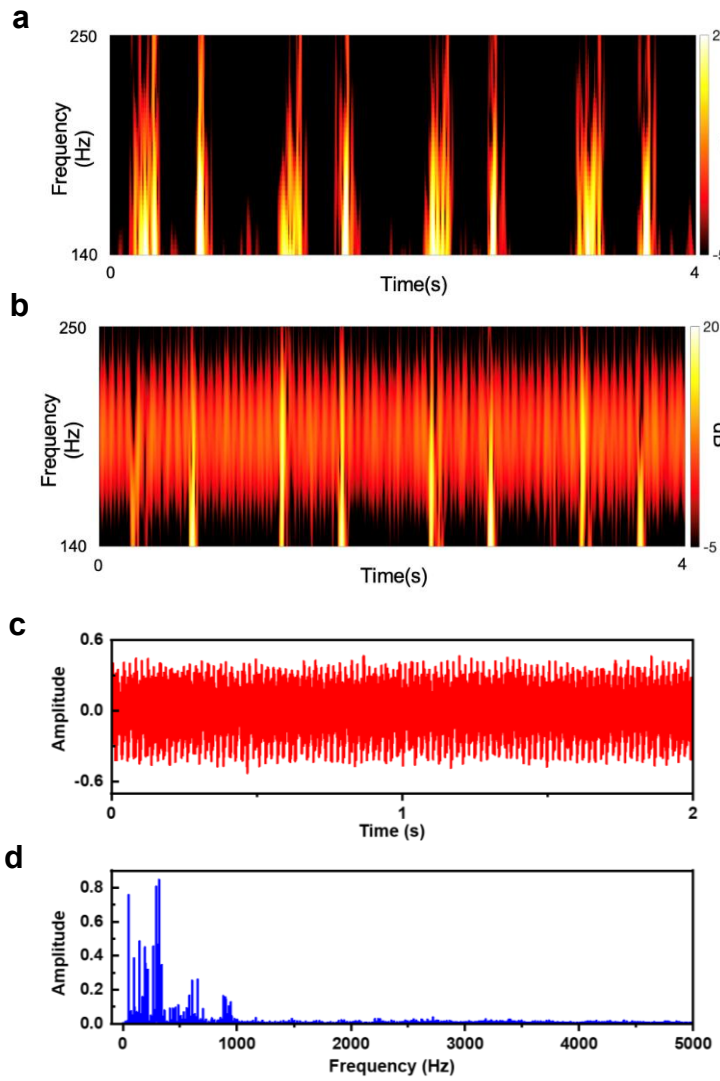

**Supplementary Figure 29. Washability of the woven fabric-integrated FCM. a**, Photographs showing each step of the wash cycle test. In each cycle, the fabric undergoes 30 minutes of machine washing at room temperature, followed by spin-drying, and is then air-dried before testing. The capacitance of the fibre is measured after each cycle to assess any potential structural damage. **b**, Capacitance values of the fibre over 10 washes. **c**, **d**, Cardiac sound monitoring using the fabric-integrated FCM before washing (**c**) and after washing (**d**), demonstrating the preservation of sensing performance and signal fidelity.



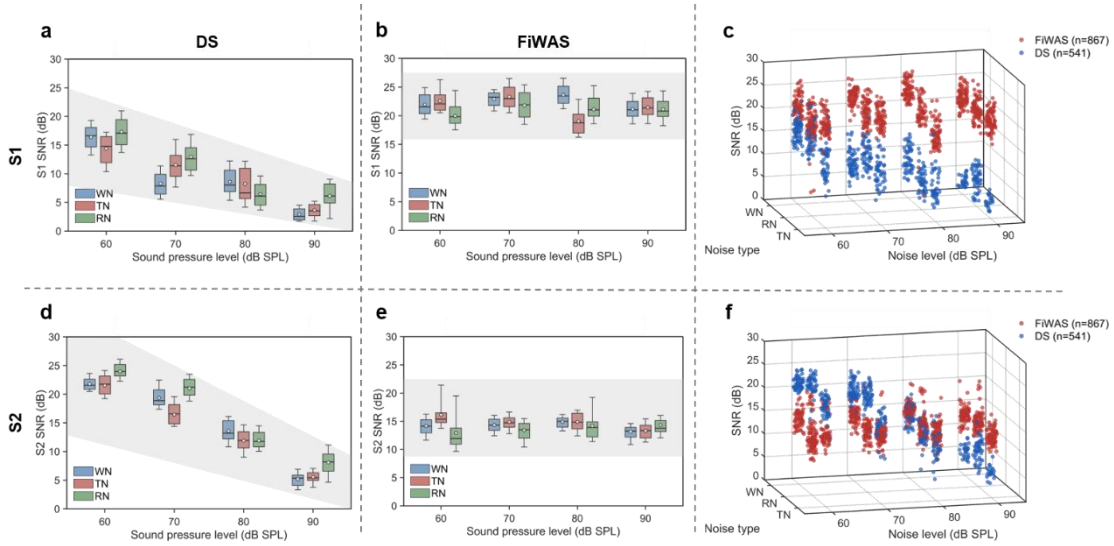

**Supplementary Figure 30. Stretchability of the fibre computer-integrated knitted fabric, showing that the knitted channel structure compresses under stretch, effectively isolating the fibre computer from unwanted mechanical strain.**



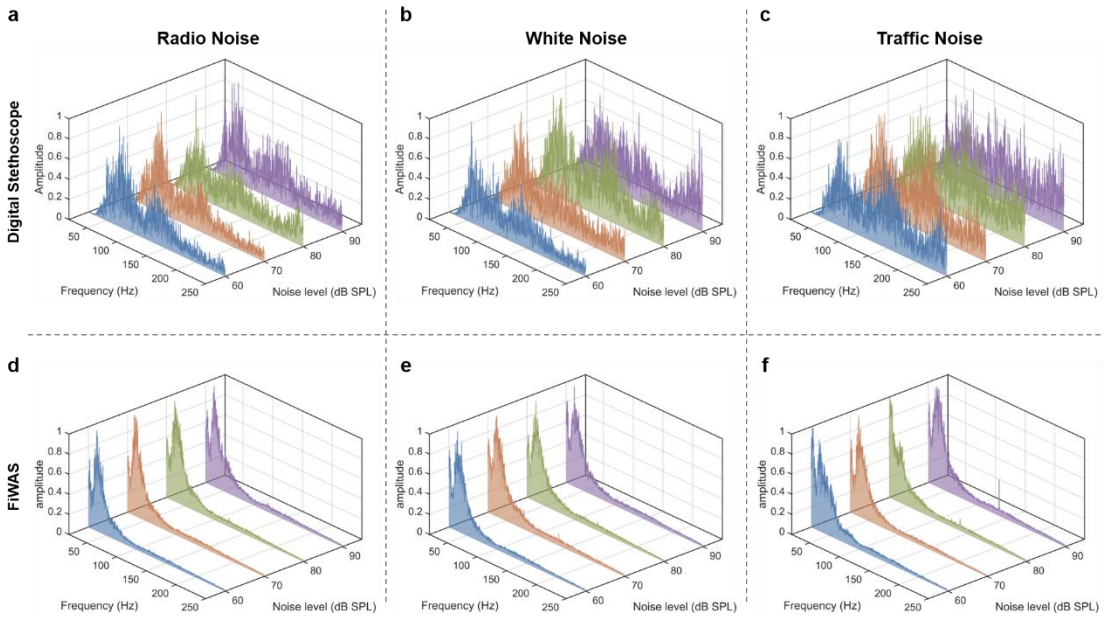

**Supplementary Figure 31. Mechanical characterization of fibre-integrated textiles.** **a,** Tensile stress–strain curves of the FCM and FC compared with conventional textile fibres. **b,** Fabric-level flexural rigidity measured by the ASTM D1388 cantilever method, indicating that the integrated textile retains low bending stiffness and fabric-level flexibility.



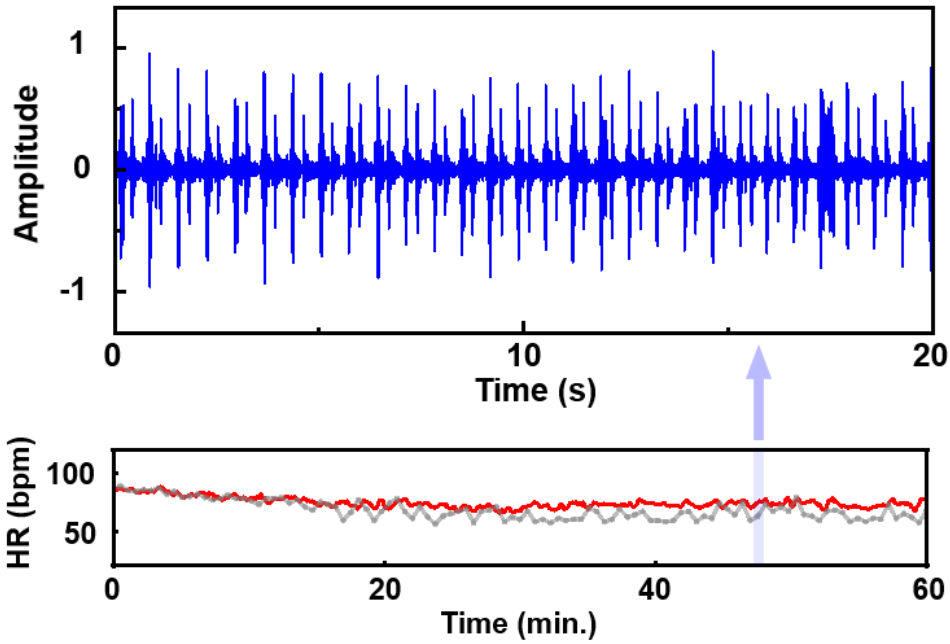

**Supplementary Figure 32. Noise interference comparison between the digital stethoscope and the fibre wireless auscultation system.** STFT graph of the cardiac sound recording from a digital stethoscope (**a**) and the system (**b**) under 90dB ambient noise from an air compressor. Waveform of the noise signal (**c**) and its frequency distribution (**d**).



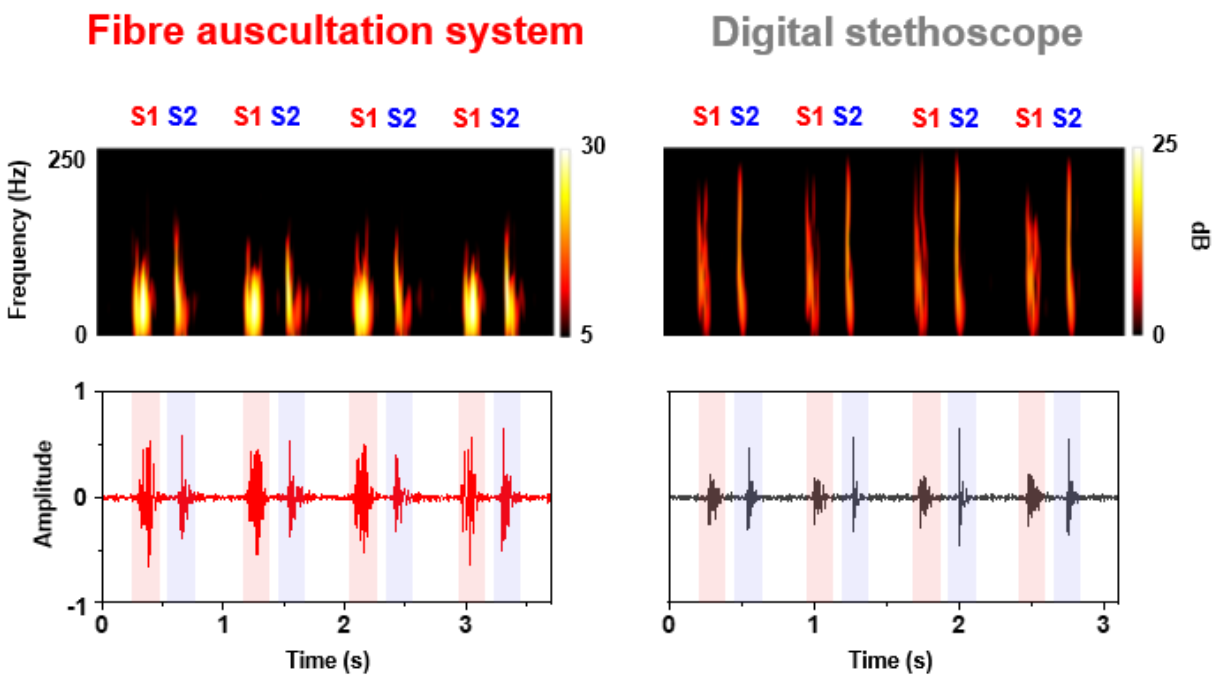

**Supplementary Figure 33. Quantitative evaluation of environmental-noise robustness. a, b,** S1 SNR measured by a commercial digital stethoscope and FiWAS under different environmental noise spectra and sound pressure levels. **c,** Cohort-level 3D distribution of S1 SNR as a function of noise type and noise level. **d, e,** S2 SNR measured by a commercial digital stethoscope and FiWAS under the same noise conditions. **f,** Cohort-level 3D distribution of S2 SNR. White noise (WN), Traffic noise (TN), and Radio noise (RN) denote three representative environmental noise spectra. Boxes indicate the 25%–75% range, the whiskers indicate the 10%–90% percentile range, the horizontal lines indicate the median, and the circles indicate the mean FiWAS for heart-sound recording under environmental acoustic noise. N denotes the number of individual SNR data points included in the analysis (n = 867 for FiWAS and n = 541 for the commercial digital stethoscope).



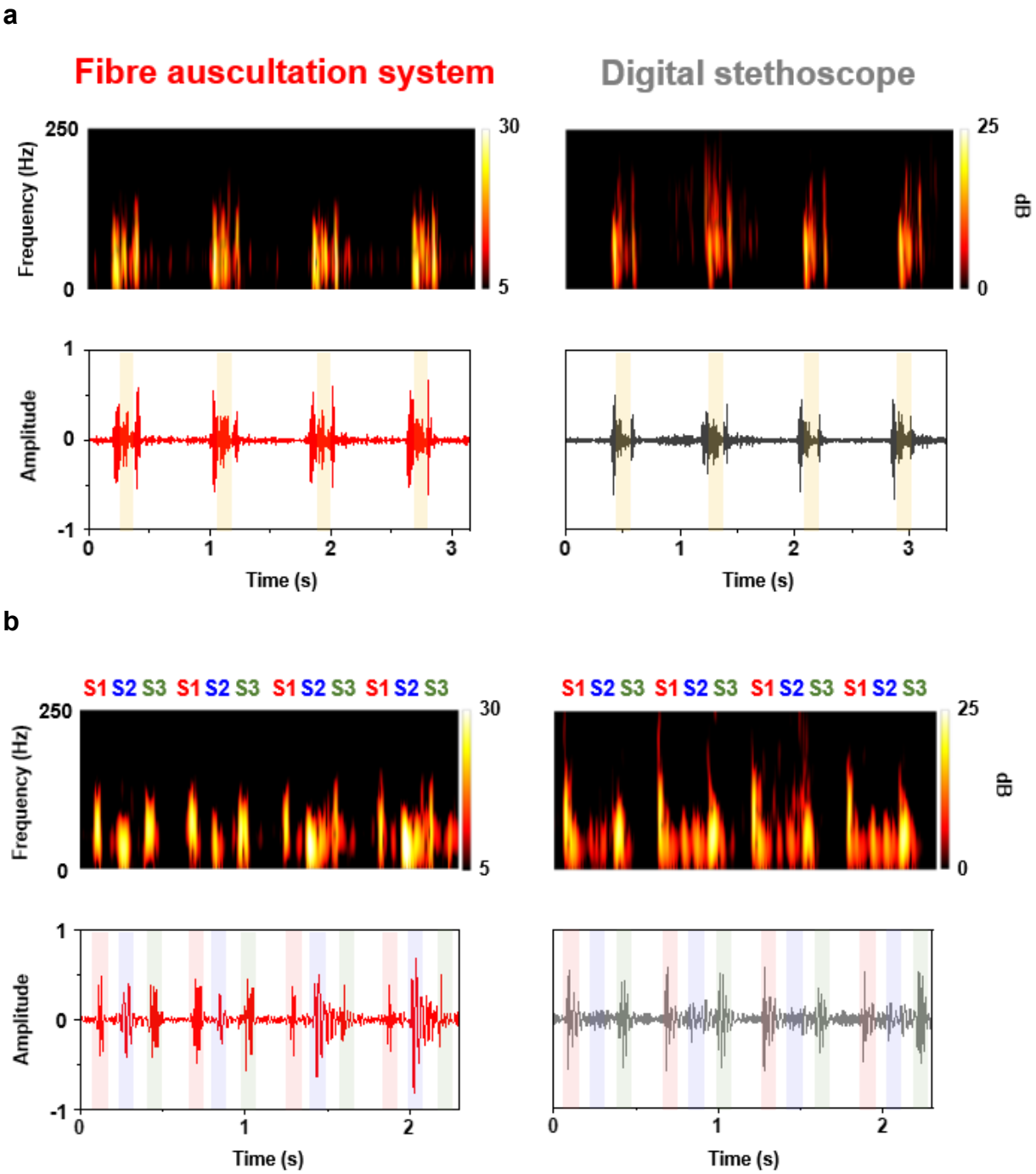

**Supplementary Figure 34. Averaged FFT analysis of heart-sound recordings under controlled environmental noise. a–c,** Averaged FFT spectra of heart-sound recordings obtained using the commercial digital stethoscope under three representative environmental noise spectra, including white noise, traffic noise, and radio noise. **d–f,** Averaged FFT spectra of heart-sound recordings obtained using FiWAS under the same noise conditions. For each panel, FFT spectra were calculated from all cardiac sound recordings under different noise levels.



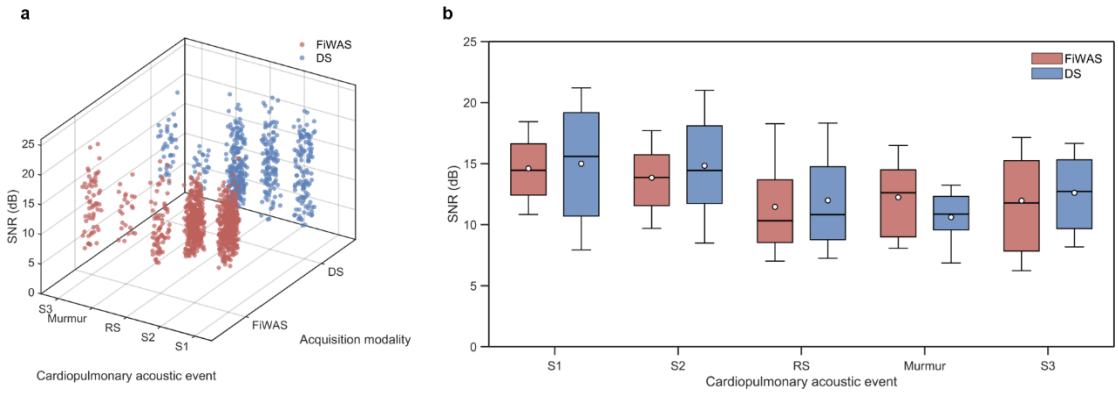

**Supplementary Figure 35. Cardiac sound recording during long-term heart rate monitoring, demonstrating the system's capability for continuous heart sound logging, enabling retrospective analysis and providing valuable diagnostic support.**



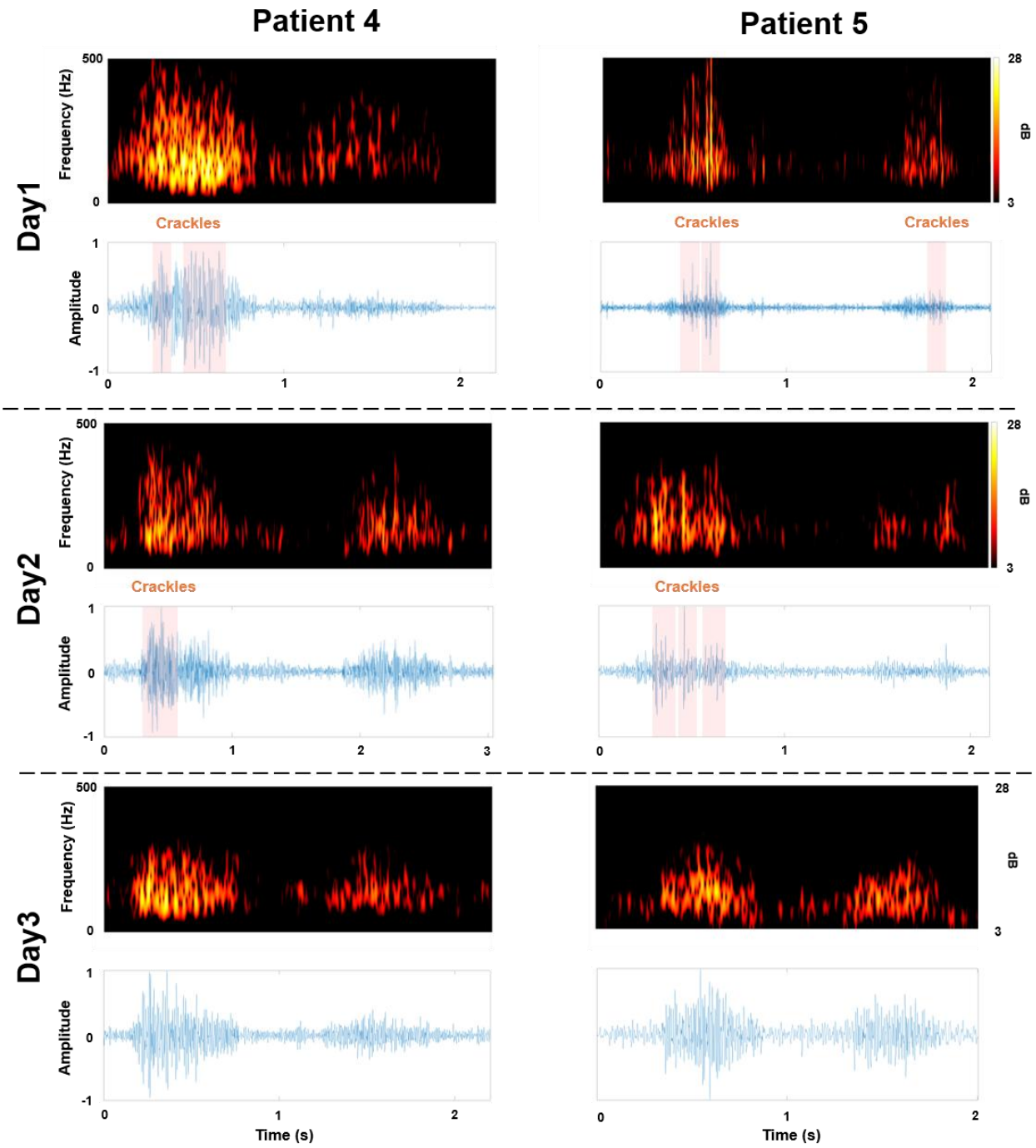

**Supplementary Figure 36. Normal heart sound (S1 and S2) comparison between fibre wireless auscultation system and digital stethoscope.**



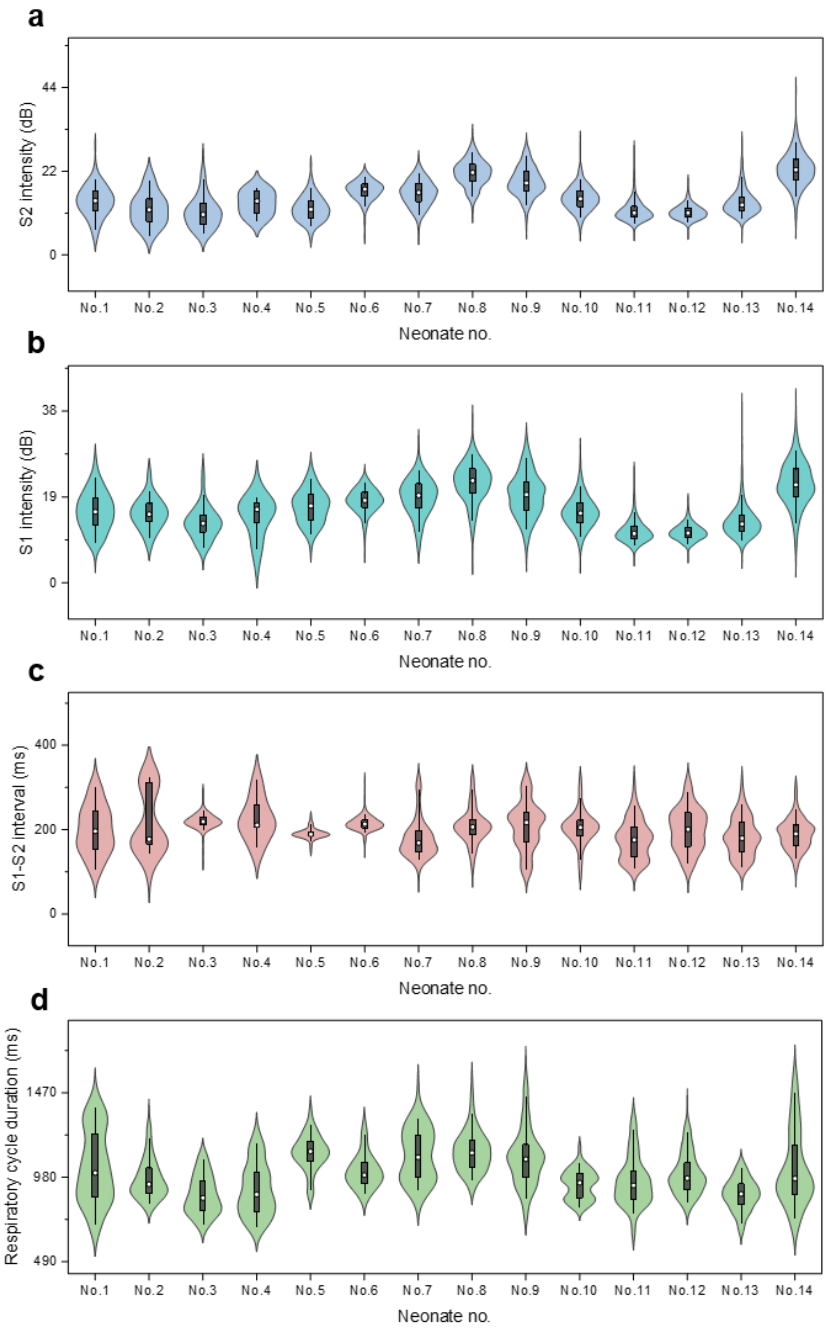

**Supplementary Figure 37. Abnormal heart sound comparison between the FiWAS and digital stethoscope. a**, Systolic murmur sound. **b**, S3 gallop.



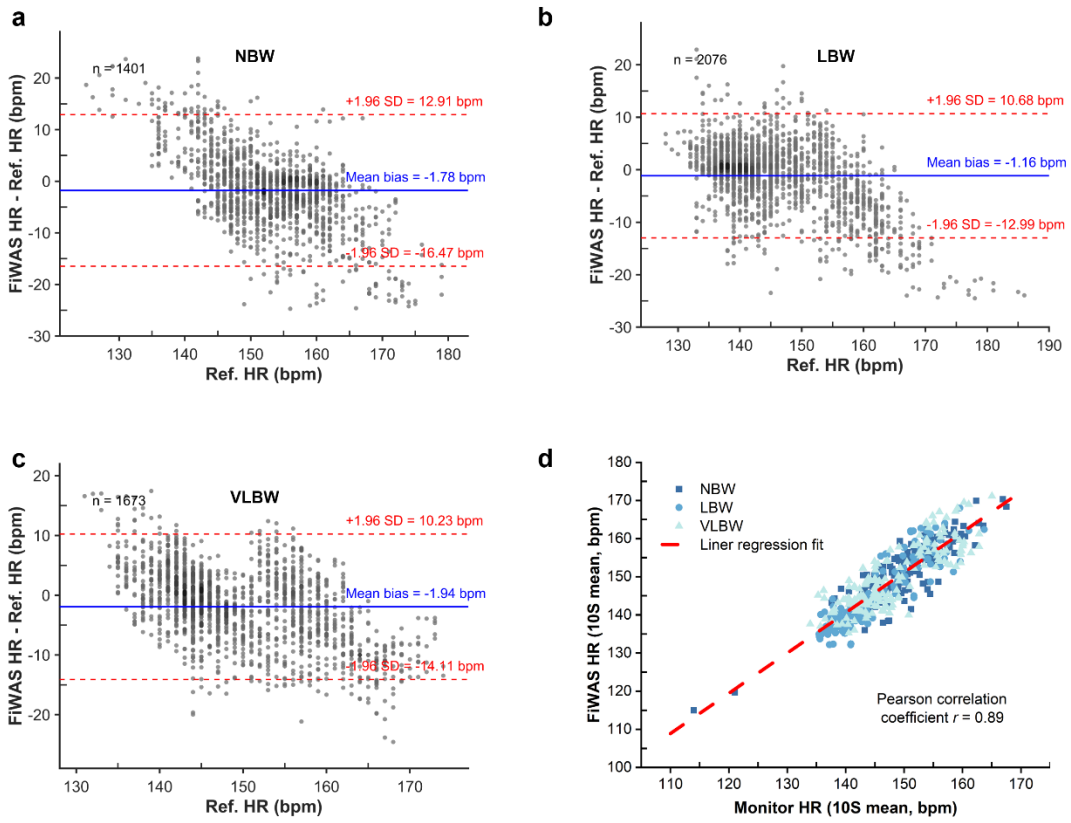

**Supplementary Figure 38. SNR comparison between FiWAS and the commercial digital stethoscope.** Three-dimensional scatter plot (**a**) and box-and-whisker plots (**b**) showing the SNR distributions of FiWAS and the commercial digital stethoscope (DS) for five cardiopulmonary acoustic events: S1, S2, respiratory sounds (RS), murmur and S3. In the box plots, the centre line indicates the median, the box bounds indicate the interquartile range (25–75%), the whiskers indicate the 10–90% range, the middle line denote the median value, and the white circles denote the mean value. S1 (FiWAS, $n$ = 359; DS, $n$ = 121), S2 (FiWAS, $n$ = 342; DS, $n$ = 117), lung sounds (FiWAS, $n$ = 70; DS, $n$ = 217), murmurs (FiWAS, $n$ = 23; DS, $n$ = 24) and S3 gallops (FiWAS, $n$ = 58; DS, $n$ = 37). Here, $n$ denotes the number of valid individual SNR measurements obtained from acoustic events or recording segments.



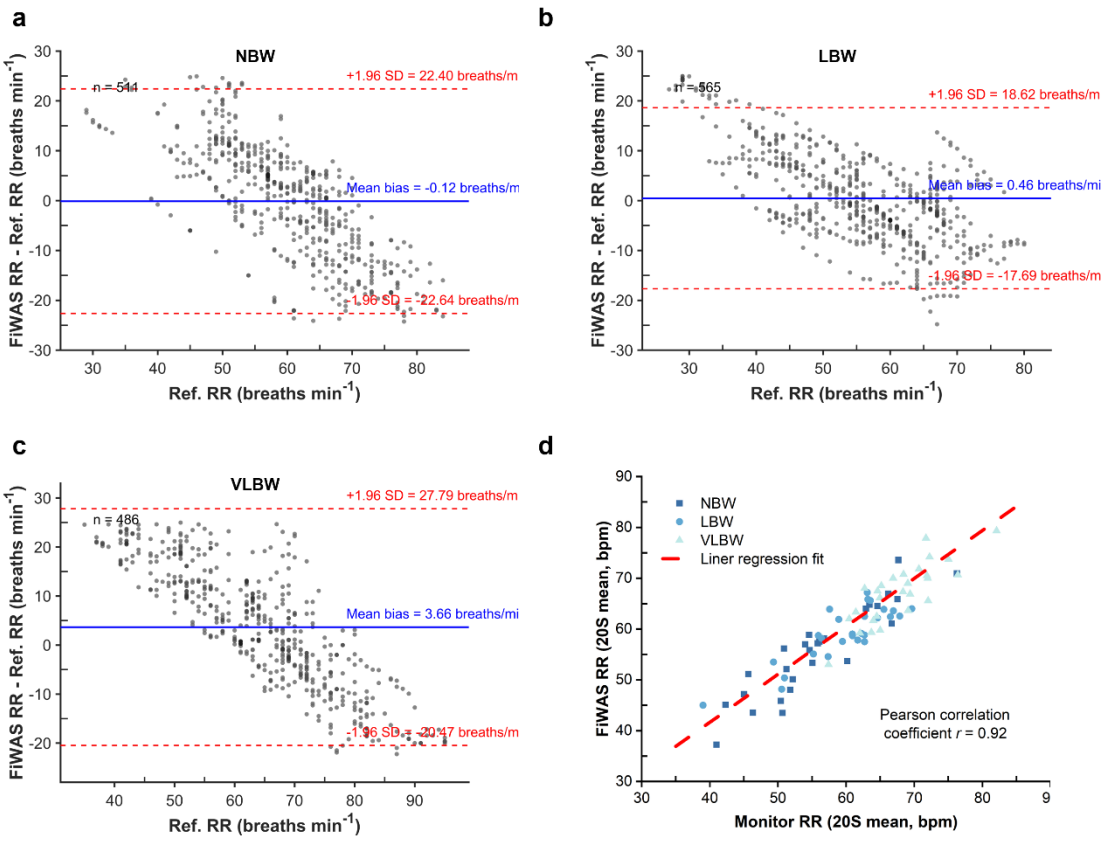

**Supplementary Figure 39. Tracking of remission of crackle symptoms during treatment, showing the reduction of crackles in the lower left posterior chest of patient 4 and in the middle left and middle right posterior chest of patient 5 during the three-day treatment period.**



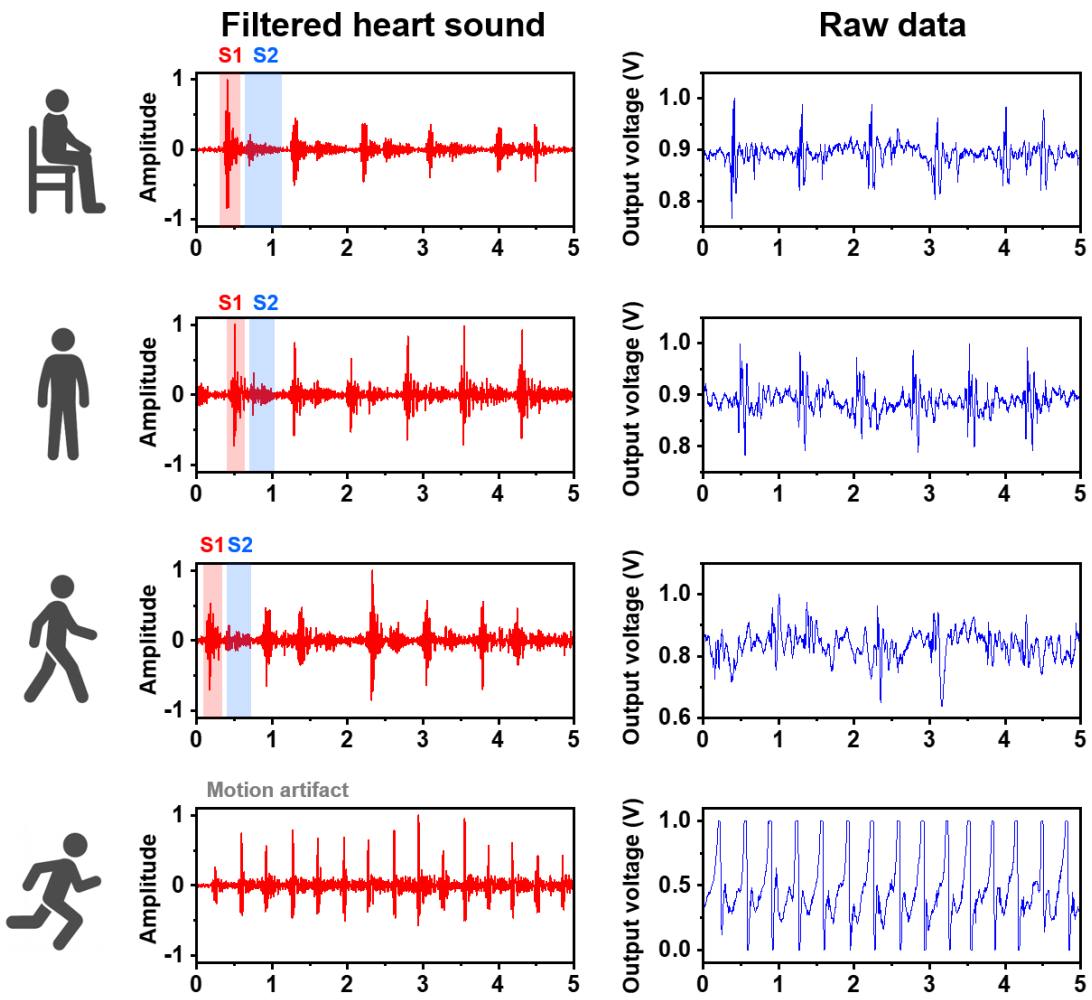

**Supplementary Figure 40. Cohort-level distributions of primary neonatal acoustic and physiological metrics measured by FiWAS in 14 SCN/NICU neonates, showing S2 intensity (a),** S1 intensity **(b),** S1–S2 interval **(c),** and respiratory cycle duration **(d)** for each individual neonate. Embedded box plots indicate the 25%-75%, whiskers indicate the 5%-95%, and the central dot denotes the median. The number of data points was n = 11893 for the heart sound-related dataset and n = 6603 for the lung sound-related dataset.



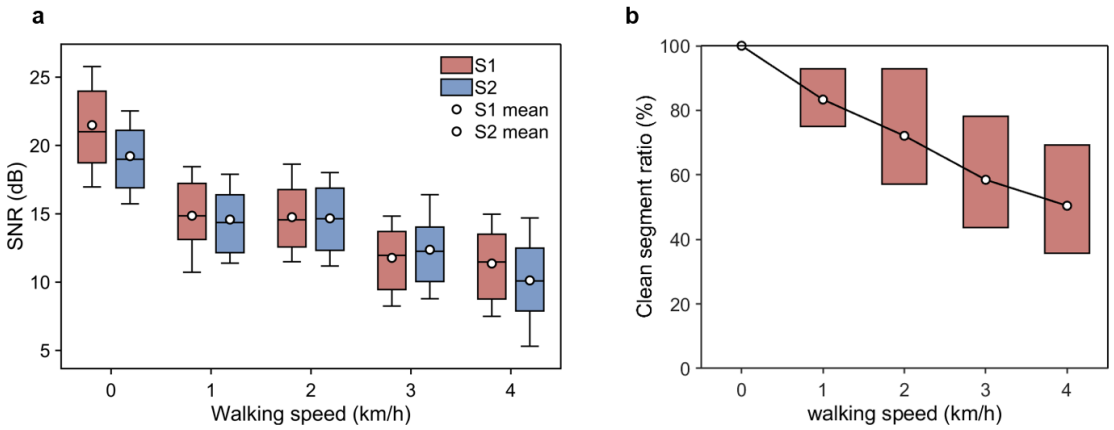

**Supplementary Figure 41. Agreement and correlation analyses of Heart Rate (HR) measurements across neonatal body-weight groups. a–c**, Bland–Altman analysis of HR measured by FiWAS relative to the clinical bedside monitor (Ref.) in normal birth weight (NBW), low birth weight (LBW), and very low birth weight (VLBW) neonates. The large standard deviations result from differences in data processing between the two systems, while the overall trends remain highly consistent. **d**, Correlation between FiWAS and monitor HR values using 10-s mean data, showing a close agreement with a Pearson correlation coefficient of 0.89. Here, n denotes the number of paired HR data points included in the Bland–Altman analyses (n = 1,401 for the NBW group, n = 2,076 for the LBW group and n = 1,673 for the VLBW group).



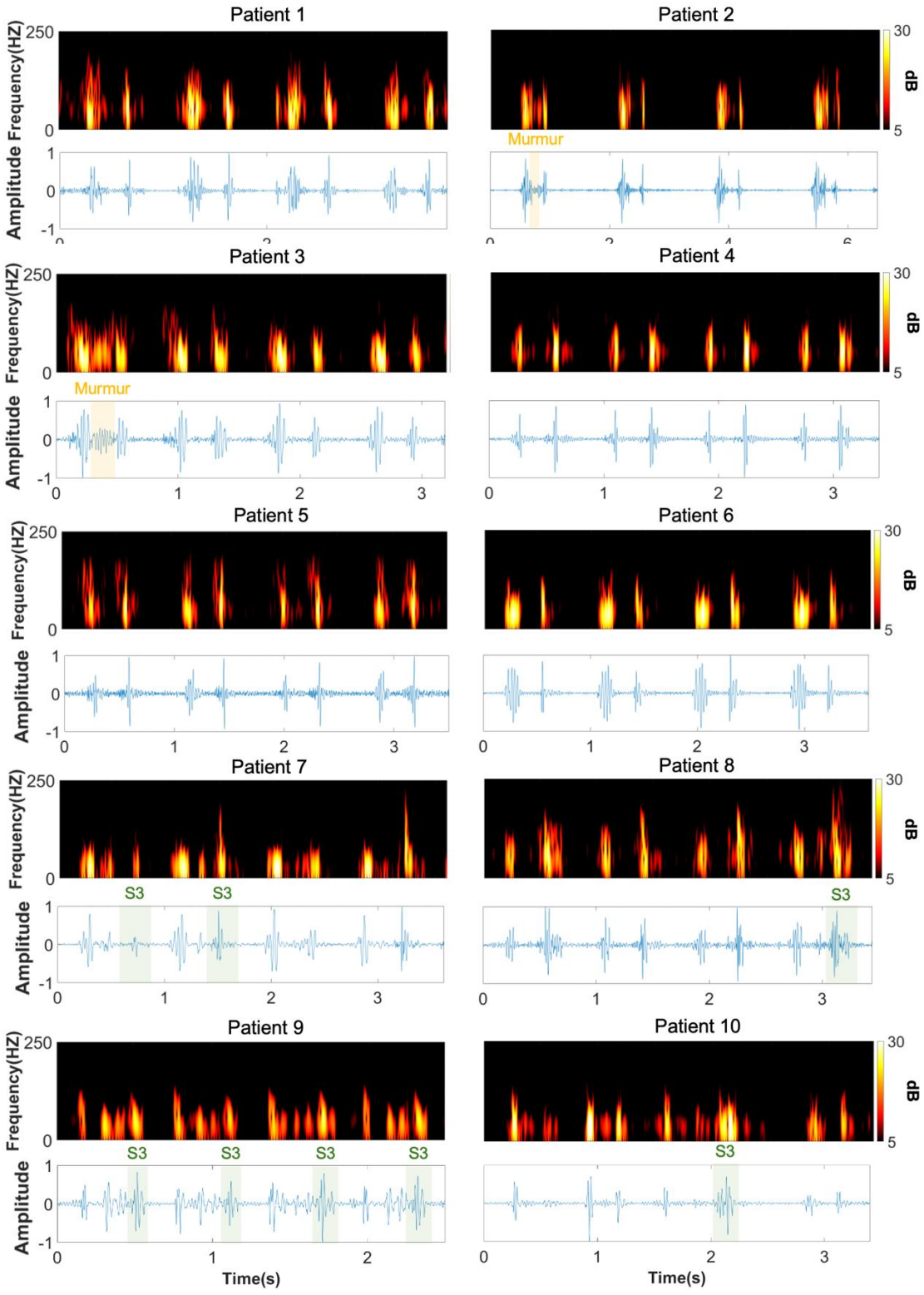

**Supplementary Figure 42. Agreement and correlation analyses of respiratory rate (RR) measurements across neonatal body-weight groups. a–c**, Bland–Altman analysis of RR measured by FiWAS relative to the clinical bedside monitor (Ref.) in normal birth weight (NBW), low birth weight (LBW), and very low birth weight (VLBW) neonates. **d**, Correlation between FiWAS and monitor RR values using 20-s mean data, showing a close agreement with a Pearson correlation coefficient of 0.92. Here, n denotes the number of paired RR data points included in the Bland–Altman analyses (n = 511 for the NBW group, n = 565 for the LBW group and n = 486 for the VLBW group).



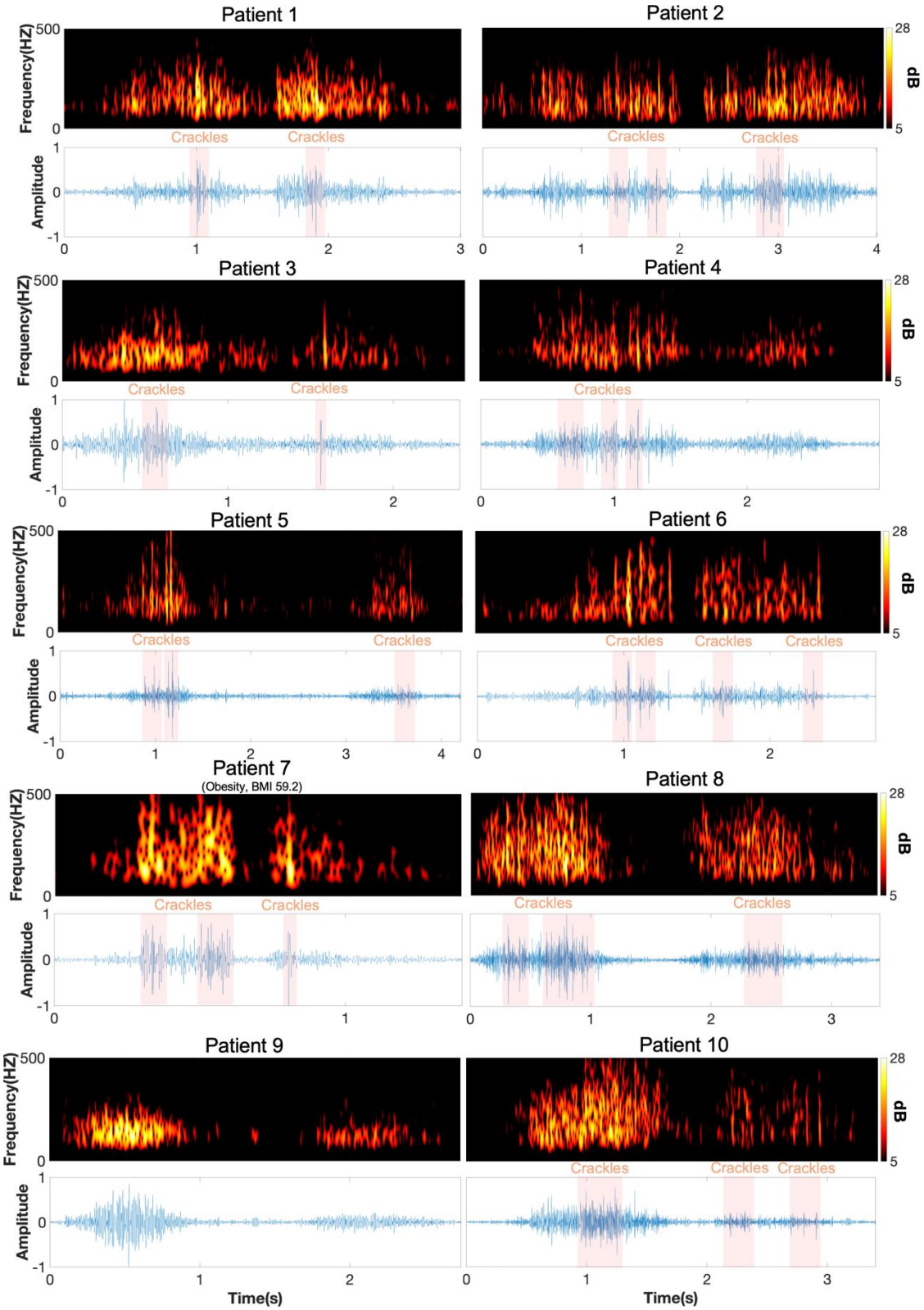

**Supplementary Figure 43. Activity-dependent influence of motion artefacts on FiWAS-recorded heart sounds in adult garment tests. Heart sound signals and corresponding raw data were recorded while the wearer was sitting, standing, walking and running. Clear S1–S2 complexes were obtained under stationary conditions, including sitting and standing. During walking, cardiac sound features remained partially recoverable but were accompanied by increased locomotion-induced artefacts, indicating an activity-dependent degradation in signal quality. During running, the signal was dominated by stride-induced motion artefacts, and reliable recovery of heart sounds was not possible.**



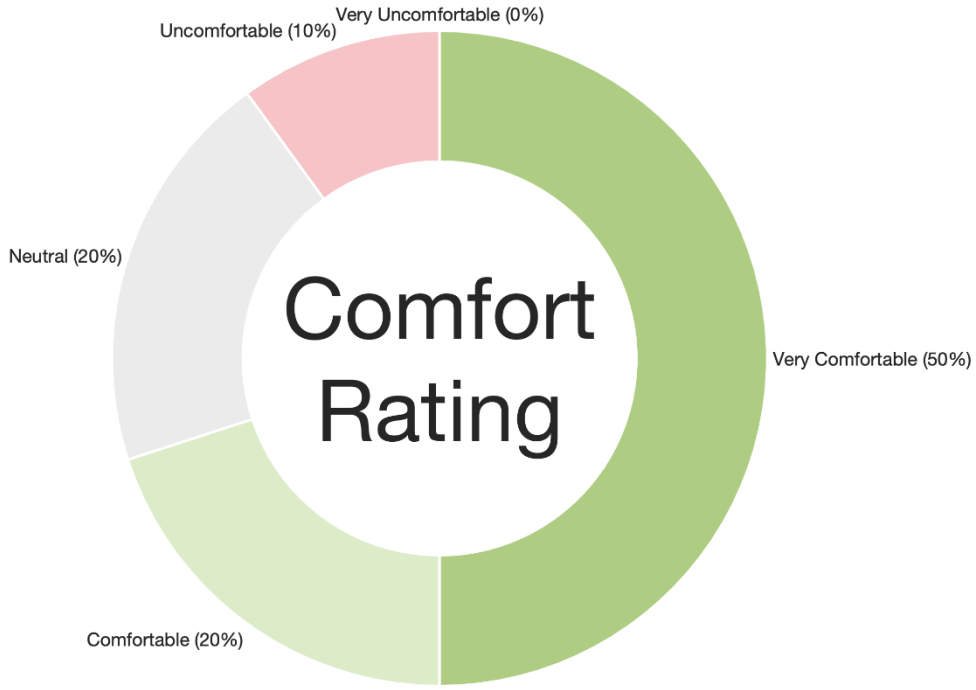

**Supplementary Figure 44. Quantitative definition of the FiWAS operating boundaries under controlled walking conditions, showing progressive reductions in both S1/S2 SNR and clean-segment ratio with increasing walking speed and demonstrating activity-dependent degradation of cardiac sound recovery under locomotion-induced motion artifacts. a**, Statistical analysis of S1 and S2 heart sound SNR recorded by FiWAS at different walking speeds. Box plots indicate the 25%–75% range, whiskers indicate the 10%–90% range, horizontal lines indicate the median, and open circles indicate the mean. **b**, Statistical analysis of the clean-segment ratio at different walking speeds. Box plots indicate the 25%–75% range, and open circles indicate the mean. At 0, 1, 2, 3 and 4 km/h, respectively, n = 42, 45, 47, 56 and 23 for each of S1 and S2 in a, and n = 15, 15, 13, 14 and 14 in b; n denotes the number of observations.



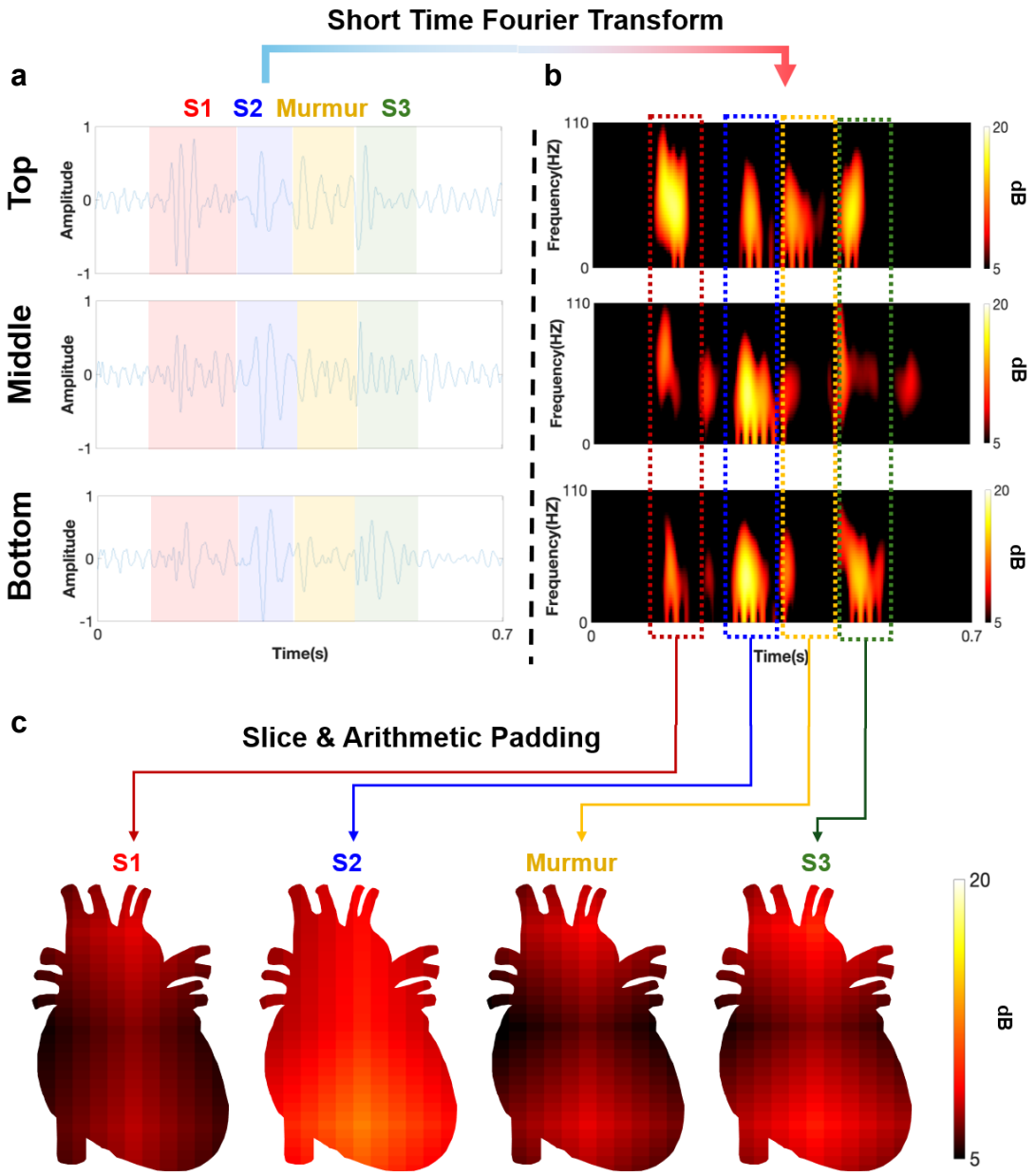

**Supplementary Figure 45. Representative cardiac sound waveforms and STFT spectrograms from ten patients in the clinical study.**




**Supplementary Figure 46. Representative respiratory sound waveforms and STFT spectrograms from ten patients in the clinical study.**




**Supplementary Figure 47. Donut chart of evaluation result from 10 patients regarding level of comfort wearing the All-Fibre Wireless Auscultation System.**




**Supplementary Figure 48. Sound intensity map process through fibre wireless auscultation system. a**, Waveforms of filtered signals corresponding to clinically significant events. b, Short-Time Fourier Transform (STFT) of the filtered signals, which aids in identifying clinical significance. **c**, Filling the 2D-projected heart heatmap by calculating key sound intensity values and interpolating using arithmetic progressions.

| Ref. | This study | Ref. 10 | Ref. 13 | Ref. 24 | Ref. 11 | Thinklabs commercial stethoscope |
|---|---|---|---|---|---|---|
| **Fibre based auscultation system** | Yes, including sensing, computing, signal transmitting | No | No | No, Fibre-form sensor only | No | No |
| **All system garment integration** | Yes, including knitting, weaving and machine sewing | No | No | No | No | No |
| **Washability** | Yes | No | No | Yes | No | No |
| **Heart Sound** | Yes | Yes | Yes | Yes | Yes | Yes |
| **Lung Sound** | Yes | Yes | Yes | No | Yes | Yes |
| **Wireless/Real-time** | Yes | Yes | Yes | No | No | No |
| **Clinical validation** | Validated with commercial digital stethoscope, and bedside patient monitor<br>10 healthy volunteers;<br>10 Heart failure patients with chronic lung disease;<br>20 neonates including preterm and NICU case. | 55 patients undergoing thoracic surgery<br>15 neonates | 20 patients with lung disease | No | No | NA |
| **Pathological findings** | S3 gallop, murmur, Crackles, arrhythmia | crackles | Crackle, wheeze, stridor, rhonchi | No | No | NA |
| **Special case** | Obese patient (BMI > 55);<br>Extreme preterm (<28 weeks);<br>Extremely low birth weight (<1000g) | No | No | No | No | NA |

**Supplementary Table 1. Comparison of wearable digital stethoscopes technology**

| Subject ID | GA weeks | Birth weight (g) | Location |
|---|---|---|---|
| 001 | 38 | 3340 | Postnatal Ward |
| 002 | 37 | 2620 | SCN |
| 003 | 40 | 4364 | Postnatal Ward |
| 004 | 39 | 3017 | Postnatal Ward |
| 005 | 30 | 1330 | SCN |
| 006 | 39 | 3528 | SCN |
| 007 | 30 | 1380 | SCN |
| 008 | 36 | 2467 | Postnatal Ward |
| 009 | 33 | 1790 | SCN |
| 010 | 27 | 940 | SCN |
| 011 | 39 | 3425 | Postnatal Ward |
| 012 | 31 | 2150 | Postnatal Ward |
| 013 | 26 | 850 | SCN |
| 014 | 30 | 1450 | NICU |
| 015 | 37 | 2425 | SCN |
| 016 | 34 | 1302 | SCN |
| 017 | 34 | 2665 | SCN |
| 018 | 32 | 1720 | SCN |
| 019 | 28 | 1130 | SCN |
| 020 | 37 | 3325 | SCN |

**Supplementary Table 2. Demographic information of the enrolled neonates**

| Patient ID | Sex | Age | Height (m) | Weight (kg) | BMI | Heart Rate (BPM) | Blood Pressure (mmHg) | Peripheral Oedema | Medication | Relevant Medical History |
|---|---|---|---|---|---|---|---|---|---|---|
| WFNHC01 | Male | 73 | 1.58 | 70.2 | 28.12 | 59 | 112/64 | Yes | Enalapril 5 mg BD; IV LASIX 60 mg BD; Bisoprolol 1.25 mg OM; Empagliflozin 10 mg OM; Tolvaptan Tablet 7.5 mg Once | Ischemic Heart Disease CABG X3; Chronic Kidney Disease G3; Congestive Cardiac Failure |
| WFNHC02 | Male | 81 | 1.71 | 71.3 | 24.38 | 54 | 124/72 | NONE | Empagliflozin 25 mg OM; Furosemide IV 40 mg BD; Apixaban 5 mg BD | Hypertension; Hyperlipidemia |
| WFNHC03 | Male | 60 | 1.60 | 64.0 | 25.00 | 90 | 149/100 | NIL | Bisoprolol 2.5 mg BD; IV Frusemide 40 mg BD | NIL Cardiac History |
| WFNHC04 | Male | 65 | 1.67 | 68.3 | 24.49 | 97 | 115/62 | NIL | IV Lasix 40 mg BD; Bisoprolol 1.25 mg OM; Empagliflozin 25 mg OM | Ischemic Heart Disease |
| WFNHC05 | Male | 70 | 1.59 | 57.2 | 22.63 | 78 | 147/82 | NONE | IV Lasix 40 mg BD; Bisoprolol 1.25 mg OM; Entresto 50 mg BD | Hypertension; Hyperlipidaemia; Diabetes Mellitus; Known Ischemic heart disease and heart failure |
| WFNHC06 | Male | 45 | 1.82 | 91.5 | 27.62 | 72 | 138/85 | NIL | IV Lasix 40 mg BD; Bisoprolol 1.25 mg OM; Dapagliflozin 10 mg OM; Aspirin 100 mg OM | Hypertension; Hyperlipidaemia; Diabetes Mellitus |
| WFNHC07 | Male | 55 | 1.74 | 156.5 | 51.69 | 94 | 106/62 | NIL | IV Lasix 40 mg BD; Bisoprolol 1.25 mg OM; Entresto 50 mg BD; IV Tazocin | Congestive Cardiac Failure; Obesity |
| WFNHC08 | Male | 79 | 1.67 | 59.4 | 21.30 | 67 | 130/76 | NIL | Frusemide IV 60 mg BD; Aspirin 100 mg OM; Amiodarone 200 mg OM; Isosorbide Dinitrate 10 mg TDS | Hypertension; Chronic Kidney Disease; Diabetes Mellitus |
| WFNHC09 | Male | 51 | 1.76 | 63.0 | 20.34 | 94 | 151/82 | NIL | Lasix 40 mg OM PO; Bisoprolol 1.15 mg OM; Entresto 50 mg 0.5 tablet BD; Plavix 75 mg OM; Metformin 500 mg BD | 1st onset heart failure; Diabetes Mellitus; Tuberculosis |
| WFNHC10 | Male | 68 | 1.68 | 73.7 | 26.11 | 64 | 112/70 | NIL | Lasix 40 mg OD; Empagliflozin 10 mg OM; Entresto 100 mg BD; Spironolactone 12.5 mg OM; Digoxin 62.5 mg EOM | Atrial Fibrillation |

**Supplementary Table 3. Patient medical history and treatment information.**

**Other Supplementary Materials:**

**Supplementary Video 1. Machine sewing of FCM**

**Supplementary Video 2. Realtime cardiac sound monitoring**

**Supplementary Video 3. Filtering test of ambient noise**

**Supplementary Video 4. Healthy cardiac Sound**

**Supplementary Video 5. Murmur cardiac Sound**

**Supplementary Video 6. Cardiac sound with S3 gallop**

**Supplementary Video 7. Healthy respiratory sound**

**Supplementary Video 8. Respiratory sound with crackles**